arXiv:2611.17614v1 [physics.flu-dyn] 13 Nov 2026

Global saddle selection and exact absolute-instability boundaries for convection in porous media with throughflow

Oleg N. Kirillov
Northumbria University, Newcastle upon Tyne, UK
oleg.kirillov@northumbria.ac.uk

Abstract

In the Darcy–Prats problem, horizontal throughflow leaves the temporal onset of convection unchanged but raises the heating required for a localized disturbance to grow at a fixed point. The saddle equations give five candidates, but only the saddles reached by deformation of the Fourier contour contribute to the growth. For $Ra > \pi^2$, $Pe > 0$ we prove that the same off-axis pair contributes throughout the domain: no Stokes transition can change its contribution. Its growth gives a unique analytic absolute threshold, first reached by the lowest vertical mode. Rescaling transfers the selection to Forchheimer drag, transverse rolls of a power-law fluid, anisotropic permeability, an open upper boundary and a vertical magnetic field. A shift of the same growth function accounts for interphase heat exchange in a model of metallic foam. At prescribed throughflow the threshold increases strictly with either resistance coefficient. In particular, a vertical magnetic field raises the absolute threshold at fixed Péclet number. Tabulated thresholds check the reduction. Algebraic elimination gives the boundary polynomial, and frequency recovery selects its physical branch. At the Darcy level the selected saddles trace an arc of the elliptic curve 11a3, a degeneration of a genus-two family at nonzero shifted levels. Series inversion on this arc gives an integer weak-throughflow series and an all-order strong-throughflow expansion. Rational certificates establish the exact convergence radii of both series on the selected sheets.

Keywords: absolute instability, saddle-point selection, Picard–Lefschetz theory, Prats problem, porous-medium convection, elliptic curves

1 Introduction

In a porous layer heated from below, buoyancy amplifies a temperature disturbance and diffusion smooths it. A horizontal throughflow, measured by the Péclet number Pe, adds advection. A disturbance may grow while it travels and still leave the region where it was created, so a growing plane wave does not mean that a fixed probe records a growing signal. Prats [1] showed that a uniform throughflow leaves the temporal onset at the Darcy–Rayleigh number $Ra = 4\pi^2$ unchanged. Spatio-temporal analysis reveals a second threshold, the transition from convective to absolute instability [2–5].

For convection in a porous layer with throughflow, Dufour and Néel [6] used a near-onset amplitude equation to study traveling rolls and fronts and to obtain the leading correction to the absolute threshold. Chung, Kim and Choi [7] derived the same weak-throughflow correction. Delache, Ouarzazi and Combarnous [8, 9] computed absolute thresholds by continuing spatial branches and compared them with experiment; see also [10, 11]. Barletta and Alves [12], Barletta and Celli [13] and the monograph of Barletta [14] made the selection mechanism explicit and turned it into a

systematic method for porous-medium convection. Some solutions of the neutral-saddle conditions must be discarded, because the corresponding contour cannot be obtained from the real Fourier contour. These works give the neutral curves, the limiting complex wavenumber, the leading coefficient c_1 at strong throughflow, and the exclusion of a spurious stationary parabola through the holomorphy obstruction of a pole, also at positive Pe. Barletta and Celli write the curve of the off-axis neutral saddles in closed polar form. Turkyilmazoglu [15] parametrizes the transverse neutral saddle locus in radicals for a vertical magnetic field, including the nonmagnetic Prats limit, and gives the frequency once the saddle is chosen. This program has also been extended by Barletta, Celli, Alves and coworkers to a power-law fluid [16], anisotropic permeability [17], anomalous diffusion [18], rectangular channels [19] and symmetric wall heat fluxes with an inclined throughflow [20]. Freitas *et al.* [21] computed absolute thresholds for a porous matrix that exchanges heat with the fluid. These studies supply independent benchmarks.

Previous studies obtained candidate thresholds by numerical saddle continuation or by explicit neutral-saddle formulae. In the numerical route one solves the three real equations $\operatorname{Re}\lambda = 0$, $\partial\lambda/\partial k = 0$ for the unknowns $(\operatorname{Re} k, \operatorname{Im} k, Ra)$, where $\lambda(k)$ is the complex growth rate of a mode $e^{\lambda t + \mathrm{i}kx}$. Several roots appear, and the smallest admissible one above the temporal onset is kept. Admissibility requires a steepest-descent deformation of the Fourier contour through the saddle without crossing a singularity [14, Sec. 3.5.3]. Suslov [22] discusses numerical continuation. Alves *et al.* [23] use adjoint sensitivities to locate candidate saddles and facilitate the causality check in differential eigenvalue problems. For the Prats problem, Barletta [14, Sec. 8.2.4, p. 190] traces the neutral pair from $Pe = 0$ and notes that in practice the contour is checked at finitely many values of Pe; see also [21]. Continuity of a saddle does not guarantee that it continues to contribute. We prove that the same pair contributes throughout $Ra > \pi^2$, $Pe > 0$, including away from the neutral curve. The largest growth rate is taken over contributing saddles [24, App. B].

Admissibility is a topological property. A saddle contributes to the large-time asymptotics of the Fourier integral when its steepest-ascent path, the cycle dual to its Lefschetz thimble, has a nonzero intersection number with the original contour [25–28]. For the simple saddles and the physical contour considered here, pinching in the sense of Briggs and Bers is the local form of this statement. In general, pointwise growth and algebraic pinched-double-root criteria must be distinguished [29]. Intersection numbers change only at Stokes phenomena or saddle coalescences [30, 31]. For the Prats family and its scaled generalizations, we prove that the contributing indices remain unchanged on the whole domain. The argument makes three selections: of the saddles by the Fourier contour (section 3), of the physical boundary by frequency recovery (section 4) and of the analytic sheets for the convergence radii (theorem 5). Table 1 compares the two routes.

Step	Saddle continuation with admissibility checks	This work
Saddles	Newton solution of $\operatorname{Re}\lambda = \partial\lambda/\partial k = 0$ at each $(Pe, \dots)$	all five saddles classified once for the whole domain (section 3.1)
Admissibility	holomorphy requirement checked on contour plots at selected Pe; criteria $Ra > 0$, $Ra > Ra_c$	intersection indices proved constant on the whole domain (lemma 1, theorem 2)
Threshold	root of the selected branch, computed separately for each model	unique root of one monotone growth function for the whole class (theorem 3, proposition 4)
Closed forms	c_1, limiting wavenumber, polar and radical formulae for neutral saddles	exact boundary polynomial with physical branch selection; elliptic model and all-order expansions; certified radii

Table 1: The established route to absolute thresholds, used to obtain the published thresholds considered here, and what the global selection adds.

Theorem 2 classifies all five complex saddles of the Prats problem for all $Ra > \pi^2$, $Pe >$

0. The selected pair defines a growth function whose zero set is a unique, analytic and strictly increasing threshold, with the lowest vertical mode minimizing it (theorem 3). Section 3.5 separates three sources of ambiguity: noncontributing saddles, roots introduced by frequency elimination and neutral imaginary saddles below the threshold. Algebraic elimination with frequency recovery gives the exact boundary and its crossing with the spurious parabola, $Pe_\times = \frac{\pi}{2}\sqrt{71 + 17\sqrt{17}}$ (section 4). A change of scale reduces Forchheimer drag, power-law transverse rolls, anisotropic permeability, an open upper boundary, vertical magnetic resistance and interphase heat exchange to levels s of one growth function. Each threshold is a single monotone root (section 5, algorithm 1), and increases with either resistance coefficient at prescribed throughflow (section 5.7). For $s = 0$ the selected neutral saddles lie on the elliptic curve 11a3, a degeneration of a genus-two family for $s \neq 0$. On this smooth model the selected arc gives all coefficients of the large-Pe series, an integer small-Pe series and certified convergence radii (section 6).

2 Wavepacket, throughflow and two thresholds

The layer is unbounded in the horizontal coordinate x and bounded by walls at $Z = 0, 1$. The walls are impermeable and isothermal, and the lower wall is hotter. The basic state is a uniform horizontal throughflow with a linear temperature profile. The temperature perturbation θ is measured from this profile, and the stream function ψ describes the velocity perturbation. The fluid moves through the pores of a fixed solid matrix under an imposed horizontal pressure gradient (figure 1). In the basic state the temperature varies only vertically, so the throughflow does not advect its gradient.

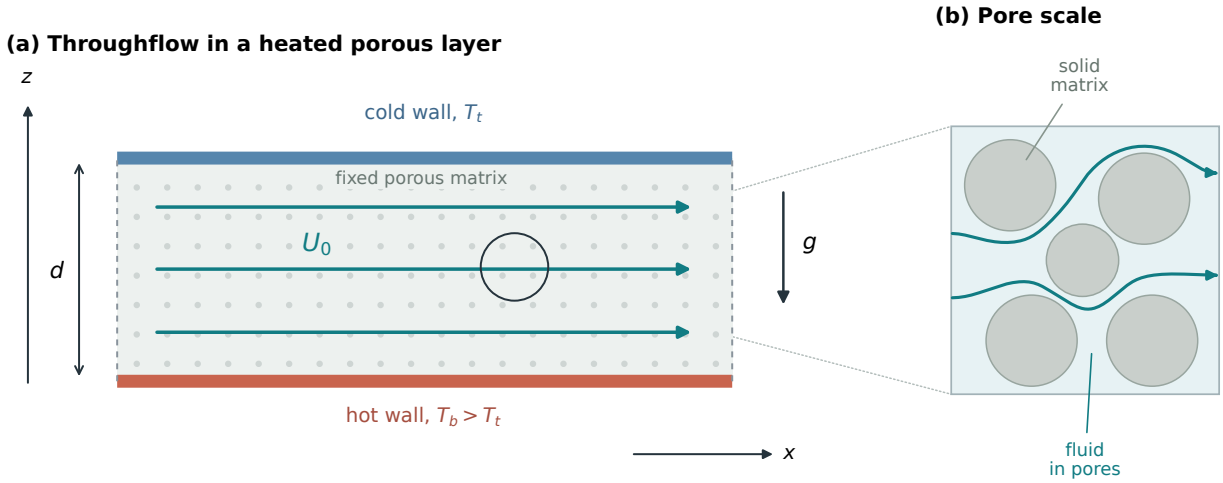


Figure 1: Physical model. (a) A section of a horizontally unbounded porous layer of thickness d. The fluid seeps to the right with mean Darcy velocity U_0; the lower impermeable wall is hotter than the upper one, and gravity points downwards. (b) Close-up: the fluid flows through connected pores between fixed grains. Streamlines are schematic; the Darcy model averages the pore structure. The equations use the dimensionless height $Z = z/d$. The figure was drawn with the AI-assisted Python code described under Computational methods.

With the thermal time scale the linear equations read

$$\nabla^2\psi = -Ra\,\partial_x\theta, \qquad \partial_t\theta + Pe\,\partial_x\theta + \partial_x\psi = \nabla^2\theta, \tag{1}$$

where Ra and Pe are the Darcy–Rayleigh and Péclet numbers, respectively.

A positive heat-capacity factor is absorbed in the time scale, and the conventions follow [12, 14]. The first equation is the instantaneous Darcy response of the velocity to buoyancy. In the second, the advection of the basic temperature gradient competes with diffusion and horizontal drift. The mode $(\psi, \theta) \propto \sin(m\pi Z)\, e^{\lambda t + \mathrm{i}kx}$, $m = 1, 2, \ldots$, with complex growth rate λ gives the exact dispersion relation

$$\lambda_m(k) = Ra \frac{k^2}{k^2 + m^2\pi^2} - (k^2 + m^2\pi^2) - \mathrm{i}Pek. \tag{2}$$

The fraction, which comes from eliminating the stream function, describes buoyant amplification. The second term is diffusive loss and the third is advection of the packet.

2.1 Temporal threshold

For a real wavenumber the advection term in (2) is purely imaginary: $\operatorname{Im}\lambda_1(k) = -Pe\,k$ only shifts the frequency, and the temporal growth rate of the first mode is $\sigma(k) = \operatorname{Re}\lambda_1(k) = Ra\,k^2/(k^2 + \pi^2) - (k^2 + \pi^2)$. Its maximum over real k is

$$\sigma_{\max} = Ra - 2\pi\sqrt{Ra}, \qquad k^2_{\max} = \pi\sqrt{Ra} - \pi^2, \qquad Ra > \pi^2, \tag{3}$$

while for $Ra \le \pi^2$ the maximum $-\pi^2$ is attained at $k = 0$. Temporal instability therefore starts at $Ra = 4\pi^2$, independently of Pe: the throughflow changes the frequencies of real waves but not their growth rates.

A localized disturbance requires the sum over all real wavenumbers. The temperature Green function of the first mode contains

$$G(x, t) = \frac{1}{2\pi} \int_{\mathbb{R}} e^{\lambda_1(k)t + \mathrm{i}kx}\, dk. \tag{4}$$

On the ray $x = vt$ the integrand of (4) becomes $e^{t\lambda_v(k)}$, where

$$\lambda_v(k) = \lambda_1(k) + \mathrm{i}vk = Ra \frac{k^2}{k^2 + \pi^2} - (k^2 + \pi^2) - \mathrm{i}(Pe - v)k$$

is the complex growth rate seen by an observer moving with speed v; $v = 0$ corresponds to a fixed probe. Let

$$S(v) = \limsup_{t\to\infty} \frac{1}{t} \log|G(vt, t)|$$

be the exponential rate along the ray. The lim sup (equivalently, a local norm over a bounded window) accounts for the oscillatory zeros produced by conjugate contributions [29]. If $S(0) > 0$ the packet grows at a fixed point and the instability is absolute; if $S(0) < 0$ but $S(v) > 0$ in some moving frame, it is convective. Since a change of observer only replaces Pe by $Pe - v$, the spreading of the packet and the absolute threshold are described by one function. Figure 2 shows both outcomes at the same heating. The spatial response of the same flow to a time-periodic source is studied by Barletta [32].

For $Ra > 4\pi^2$, $S(v)$ is positive on an interval of observer speeds centered at $v = Pe$ (figure 2(b)). The ends of this interval are the edges of the growing packet. The instability is absolute when the interval contains $v = 0$, so the trailing edge moves upstream. A stationary trailing edge marks the threshold. At $Ra = 95$ and $Pe = 20$ (point A in figure 2(a)) the fixed point lies inside the growing packet, and $S(0) = 2.2195$. At the same heating and $Pe = 50$ (point B) the whole packet is swept downstream. Both cases have the same maximal temporal growth rate. Section 3.4 shows that the interval is $|Pe - v| < c_*(Ra)$ with a unique speed c_*.

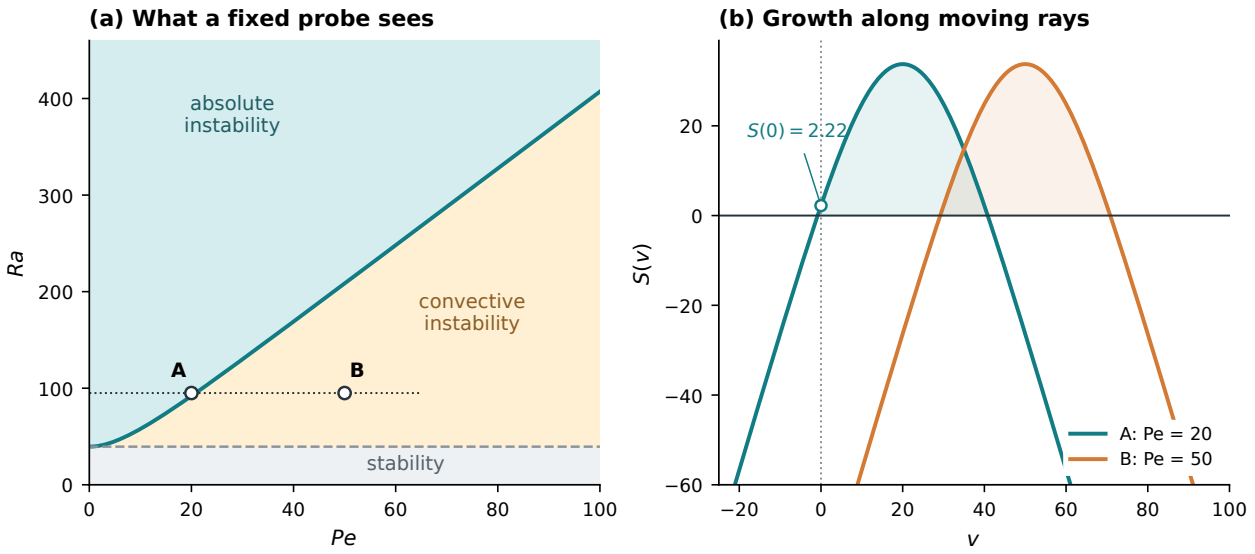


Figure 2: Drift of a growing packet. (a) The temporal threshold $4\pi^2$ and the absolute threshold separate three regions. Points A and B share $Ra = 95$ but have different throughflows. (b) At $Pe = 20$ the fixed point lies inside the growing packet, $S(0) = 2.2195$; at $Pe = 50$ the whole packet is swept downstream. The maximal temporal growth is the same. The figure was drawn with the AI-assisted Python code described under Computational methods.

2.2 Canonical variables

For the first mode and an observer moving with speed v we introduce

$$\kappa = \frac{k}{\pi}, \quad r = \frac{Ra}{\pi^2}, \quad p = \frac{|Pe - v|}{\pi}, \quad \Lambda = \frac{\lambda_v}{\pi^2}, \tag{5}$$

so that Λ is the complex growth rate λ_v in units of π^2. A reflection of the horizontal coordinate allows $p > 0$. The normalized symbol is

$$L(\kappa; r, p) = r\frac{\kappa^2}{1+\kappa^2} - (1+\kappa^2) - \mathrm{i}p\kappa. \tag{6}$$

Multiplying $\Lambda - L = 0$ by the denominator gives the spatial quartic

$$D(\kappa, \Lambda) = (\Lambda + 1 + \kappa^2 + \mathrm{i}p\kappa)(1+\kappa^2) - r\kappa^2. \tag{7}$$

For a localized disturbance the relevant stationary points lie in the complex wavenumber plane, and one must decide which complex saddles, the zeros of $L_\kappa = \partial L/\partial\kappa$, take part in the original Fourier integral (a subscript κ, r or p on L, D, F or g denotes a partial derivative, as in L_κ, $D_{\kappa\kappa}$, F_r and g_p, and a prime denotes the derivative of a function of one variable, as in $r_0'(p)$; all other subscripts are labels). Table 2 relates the canonical variables to the notation of [12, 14]. Its lower block lists the notation introduced in section 5 for the general symbol.

3 Five saddles and global selection

We prove that on the whole domain $r > 1$, $p > 0$ the physical growth is determined by the same pair of saddles. The domain $r \le 1$ needs no analysis: on the real contour $\mathrm{Re}\, L \le -1$, so a localized disturbance cannot grow absolutely.

Symbol	Meaning	Canonical variable
Ra (R in [14])	Darcy–Rayleigh number	$r = Ra/\pi^2$
Pe; v	Péclet number of the throughflow; speed of the observer	$p = \lvert Pe - v\rvert/\pi$
k	horizontal wavenumber	$\kappa = k/\pi$
λ; $\lambda_v = \lambda + \mathrm{i}vk$	complex growth rate in the laboratory frame and for an observer moving with speed v ($\mathrm{Re}\,\lambda = \sigma$ for real k)	$\Lambda = \lambda_v/\pi^2$
Introduced in section 5 for the general symbol (26)		
$\mathcal{R}$, $\mathcal{P}$	buoyancy and advection parameters	$r = \mathcal{R}/(A\pi^2)$, $p = \mathcal{P}/\alpha$
A, B	coefficients of the buoyancy denominator $A\pi^2 + Bk^2$	$\alpha = \pi\sqrt{A/B}$, $\kappa = k/\alpha$
s	level of the shifted problem, $s = B/A - 1 > -1$	$s = 0$ for Darcy
$g(r,p)$	canonical growth rate of the selected saddle (theorem 2)	threshold $g(r,p) = s$

Table 2: Notation. Upper block: variables of [12, 14] and the canonical variables (5) of the Darcy–Prats problem. Lower block: notation of section 5, which reduces to the upper block for $A = B = 1$.

3.1 Location of the saddles

The saddles are the zeros of $L_\kappa = 2r\kappa/(1+\kappa^2)^2 - 2\kappa - \mathrm{i}p$. Multiplied by $-(1+\kappa^2)^2$, which does not vanish away from the poles $\kappa = \pm\mathrm{i}$, the stationarity condition $L_\kappa = 0$ becomes the quintic

$$(2\kappa + \mathrm{i}p)(1+\kappa^2)^2 - 2r\kappa = 0. \tag{8}$$

Its five roots are shown in figure 3(a) for $Pe = 20$ on the threshold. Equivalently, κ is a double root of the spatial quartic: along $\Lambda = L(\kappa)$ one has $D_\kappa = -(1+\kappa^2)L_\kappa$, so $D = D_\kappa = 0$ exactly at the zeros of (8).

For a saddle on the imaginary axis, $\kappa = \mathrm{i}y$, it becomes the real equation

$$p = 2y\left[\frac{r}{(1-y^2)^2} - 1\right]. \tag{9}$$

The y-derivative of the right-hand side, $2r(1+3y^2)(1-y^2)^{-3} - 2$, is positive inside $(-1,1)$ and negative on each outer interval when $r > 1$. The limiting values show that there are exactly three simple imaginary saddles,

$$\kappa_- = \mathrm{i}y_-, \quad \kappa_0 = \mathrm{i}y_0, \quad \kappa_+ = \mathrm{i}y_+, \qquad y_- < -1 < 0 < y_0 < 1 < y_+. \tag{10}$$

The remaining two roots are symmetric with respect to the imaginary axis,

$$\kappa_* = x_* - \mathrm{i}\eta, \qquad -\overline{\kappa_*}, \qquad x_*, \eta > 0. \tag{11}$$

As $p \downarrow 0$ they emerge from the real maxima $\kappa = \pm\sqrt{\sqrt{r} - 1}$. They cannot cross the real axis, where $\mathrm{Im}\,L_\kappa = -p \neq 0$, and they cannot merge on the imaginary axis, because the three solutions of (9) are simple. All five saddles are therefore simple on the whole domain. Figure 3(a) shows them at $Pe = 20$ on the threshold: the pair (11) as filled circles and the imaginary saddles (10) as open circles.

Each saddle is a square-root branch point of the spatial roots $\kappa(\Lambda)$, or a spatial exceptional point of order two (EP2) [33]. A branch point contributes only when the Fourier contour admits the appropriate steepest-descent deformation [34].

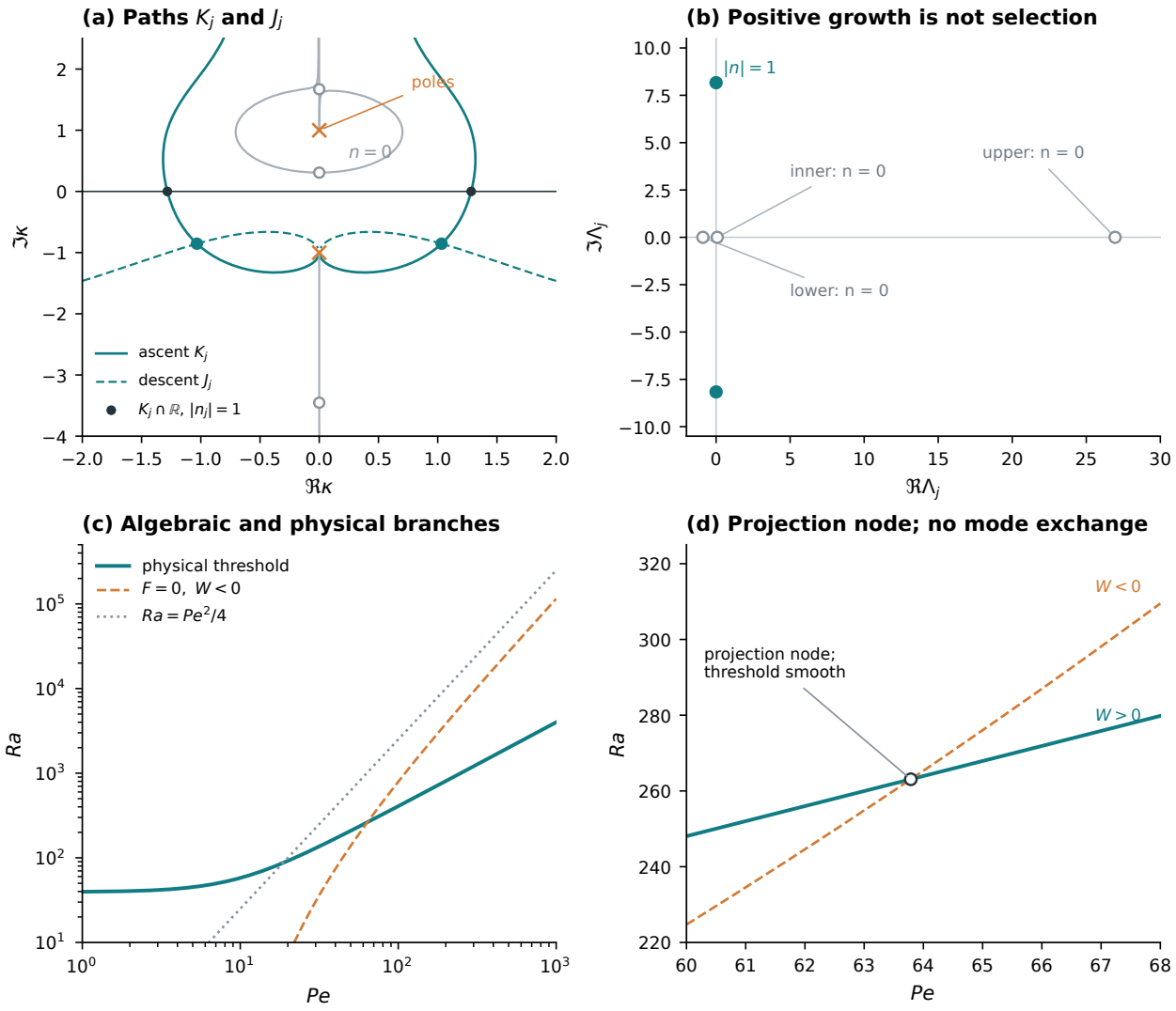


Figure 3: Selection and its algebraic trace. (a,b) At $Pe = 20$, $Ra = 91.952768$: physical saddles filled, imaginary saddles open, poles marked by crosses; panel (a) shows the steepest-ascent paths K_j of all five saddles (solid) and the steepest-descent paths J_j of the off-axis pair (dashed); dots mark the single crossing of each K_j of the pair with the real contour. For the aligned imaginary saddles the ray is tilted sideways by 0.002. (b) Critical values $\Lambda_j = L(\kappa_j)$ of the five saddles: on the threshold the off-axis pair has $\Lambda_j = \mp 8.165\,\mathrm{i}$, a purely oscillatory response, whereas the inner and upper imaginary saddles have positive real critical values, 0.079 and 26.945, but zero index; the lower one has -0.890. A larger growth does not select a saddle. (c) Physical boundary, the extra real branch of $F(r, P) = 0$, and the spurious parabola. Here $P = p^2/4$, and F is the boundary polynomial introduced in section 4, equation (21). On the extra branch the squared frequency $W = \Omega^2$ of the neutral wave $\Lambda = \mathrm{i}\Omega$ is negative, so it carries no real oscillation. (d) Projection node: the physical threshold passes smoothly because the second branch has $W < 0$. The figure was drawn with the AI-assisted Python code described under Computational methods.

3.2 How a saddle enters the Green function

A root of the quintic does not by itself determine the growth of the packet. From the critical value $\Lambda_j = L(\kappa_j)$, the value of L at the saddle κ_j, we lift the ray $\Lambda = \Lambda_j + \rho$, $\rho \geq 0$, to the surface $D = 0$. Two spatial branches are born from the double root, and their position relative to the original real contour decides whether the saddle enters the Green function. Equivalently, let J_j be the steepest-descent path through the saddle, its Lefschetz thimble, and K_j the steepest-ascent path, the dual cycle [25–27]. The coefficient of the saddle in the decomposition of the real contour is the oriented intersection number $n_j = \langle \mathbb{R}, K_j \rangle$: $n_j = 0$ means no contribution and $|n_j| = 1$ one contribution to the deformed contour. Figure 3(a) shows these paths at $Pe = 20$: each ascending path of the off-axis pair crosses the real axis once, while those of the imaginary saddles do not cross it. The same contour coefficient defines an active saddle in the waveguide analysis of Shanin, Korolkov and Kniazeva [35]. Their test follows the two reverse steepest-descent streams and accounts for cancellation when they hit the initial contour with opposite orientations. The zero level used in their test relies on a real phase on that contour. Here the physical Fourier contour has nonconstant $\operatorname{Re} L$, and we use its oriented intersection with K_j directly.

Lingwood [36] compares the Briggs test with steepest descent and gives examples of saddles that the deformed Fourier contour cannot reach. In the construction of Briggs and Bers, the two spatial branches that merge in a contributing saddle lie on opposite sides of the real κ-axis when $\operatorname{Re}\Lambda$ is large, before the Laplace contour is lowered [2–4]. If the temporal symbol $\lambda(k)$ is a polynomial in k, all spatial roots tend to infinity as $\operatorname{Re}\Lambda \to +\infty$, so the two sides correspond to roots that go to infinity in opposite half-planes. The rational symbol has poles at $\kappa = \pm\mathrm{i}$: from $D = 0$, two roots tend to them, $\kappa \approx \pm\mathrm{i}\,(1 + r/2\Lambda)$, and two tend to infinity, $\kappa \approx \pm\mathrm{i}\sqrt{\Lambda}$. Each side of the contour thus receives one root from a pole and one from infinity, and the sides must be read off from the real contour rather than from the behavior at infinity.

Consider a continuous family of rational phases whose saddles remain simple. Assume that the pole orders and the decay ends, the sectors near the poles and at infinity where $\operatorname{Re} L \to -\infty$, persist, and that no saddle reaches a pole or infinity. The integration contour is then transported in the corresponding relative homology. A chosen saddle has a constant intersection index if its critical value never shares its imaginary part with another critical value [27, 28]. Indeed, $\operatorname{Im} L$ is constant along gradient trajectories, so no Stokes connection can involve that saddle. If a conjugate pair has nonreal critical values and all remaining critical values are real, both members satisfy this condition.

Lemma 1 (Invariance of the physical indices)**.** *On the domain $r > 1$, $p > 0$ the critical values of the off-axis pair have nonzero imaginary parts of opposite sign. They therefore never align with each other or with the critical value of an imaginary saddle, which is real, and the intersection indices of the off-axis pair are constant on the domain. The indices of the imaginary saddles are determined directly in the proof of theorem 2.*

Proof. Suppose the critical value of the pair were real. The symmetry $L(-\overline{\kappa}) = \overline{L(\kappa)}$ would then give two distinct double roots of the quartic at the same real Λ. With $q = |\kappa_*|^2$ and $y = \operatorname{Im}\kappa_*$ the quartic would be the perfect square $D(\kappa, \Lambda) = (\kappa^2 - 2\mathrm{i}y\kappa - q)^2$. Comparing the coefficients of κ^3 and κ requires both $p = -4y$ and $p = 4yq$, hence $q = -1$, which is impossible. Hence $\operatorname{Im} L(\kappa_*) \neq 0$, and by the symmetry the two critical values are complex conjugate. The continuation criterion above now applies: all saddles are simple (section 3.1), none reaches a pole or infinity, since the quintic (8) has the constant leading coefficient 2 and takes the value $\mp 2\mathrm{i}r \neq 0$ at $\kappa = \pm\mathrm{i}$, the parameter domain is connected, and the pole orders and decay ends persist. The indices of the pair are therefore constant. Stokes alignments between the three imaginary saddles can occur; their indices are determined directly in theorem 2. □

Theorem 2 (Global selection)**.** *For $r > 1$, $p > 0$ the three imaginary saddles have zero index and the two off-axis saddles have index of modulus one. The canonical exponential growth rate is*

$$g(r, p) = \operatorname{Re} L(\kappa_*; r, p). \tag{12}$$

In the thermal time scale of section 2, with $g(r, 0)$ defined by continuity, the rate along a moving ray is

$$S(v) = \pi^2 g\left(\frac{Ra}{\pi^2}, \frac{|Pe - v|}{\pi}\right).$$

Proof. For the outer imaginary saddles the ascending cycles lie on the imaginary axis. The axis is invariant under the gradient flow of $\operatorname{Re} L$, because the symmetry $L(-\overline{\kappa}) = \overline{L(\kappa)}$ maps it onto itself, and on it

$$L(\mathrm{i}y) = \frac{ry^2}{y^2 - 1} + y^2 - 1 + py$$

is real. On each outer interval, $y > 1$ and $y < -1$, this function has a single critical point, the saddle (section 3.1), and tends to $+\infty$ at both ends, $y \to \pm 1$ and $y \to \pm\infty$. The saddle is therefore its strict minimum, and the two ascending branches run along the axis to the pole and to infinity: to $+\mathrm{i}$ and $+\mathrm{i}\infty$ for the upper saddle, to $-\mathrm{i}$ and $-\mathrm{i}\infty$ for the lower one. Neither cycle meets the real contour, and both indices vanish. For the inner saddle stationarity gives

$$L(\mathrm{i}y_0) + 1 = y_0^2 \left[\frac{r(1 + y_0^2)}{(1 - y_0^2)^2} - 1\right] > 0. \tag{13}$$

Its critical value is real. On the real axis $\operatorname{Im} L = -p\kappa$, so a cycle with $\operatorname{Im} L = 0$ could meet the axis only at $\kappa = 0$, where $L = -1$; but $\operatorname{Re} L$ increases along an ascending cycle and cannot pass from a value larger than -1 to a smaller one. The index of the inner saddle is zero as well.

On the real axis $\operatorname{Im} L = -p\kappa$ takes a given value only once, so each ascending cycle of the pair meets it at most once. To establish a crossing, fix $r = 4$ and let $p \downarrow 0$. At $p = 0$ the positive temporal maximum is $\kappa = 1$, with $L_{\kappa\kappa} = -4$. The implicit function theorem gives

$$\kappa_*(p) = 1 - \frac{\mathrm{i}p}{4} + O(p^2), \qquad \operatorname{Im} L(\kappa_*) = -p + O(p^3).$$

The unique real point with the same value of $\operatorname{Im} L$ is $x_c = -\operatorname{Im} L(\kappa_*)/p = 1 + O(p^2)$, and

$$\operatorname{Re} L(x_c) - \operatorname{Re} L(\kappa_*) = \frac{p^2}{8} + O(p^3) > 0.$$

The holomorphic Morse lemma therefore places x_c on the local ascending cycle. Its tangent tends to the imaginary direction, so the crossing is transverse. Reflection gives the crossing for the other saddle. Hence both indices have modulus one at $r = 4$ for small positive p, and lemma 1 extends this result to the whole domain. □

Figure 3(b) shows that the height of a critical value does not decide whether a saddle contributes: two imaginary saddles have positive real critical values on the threshold, but zero index.

Direct quadrature at a fixed probe. We evaluated (4) at $x = 0$ on two lines $\kappa = \xi - \mathrm{i}c$, with $c = 3/4$ and $2/3$. No pole is crossed, and diffusion makes the connecting vertical integrals vanish at infinity. The trapezoidal rules use steps $1/64$ and $1/128$ in 55- and 65-digit arithmetic, respectively. At the $Pe = 50$ threshold and $T = \pi^2 t = 20$, the peak magnitude of e^{TL} on the shallower line exceeds

$|G(0,t)|$ by a factor of about 1.7×10^{25}, so double precision is inadequate. The two quadratures agree to within 10^{-15} of the peak sampled signal in each case. Neither computation uses the saddle locations.

We fit an exponential sinusoid to $\sqrt{T}\,G(0,t)$ on $16 \le T \le 20$, removing the leading algebraic decay before estimating the canonical growth rate and angular frequency. At point A of figure 2(a), $(Pe, Ra) = (20, 95)$, the fit gives $(0.22481, 8.27468)$, against $(0.22488, 8.27465)$ for the off-axis pair. The upper imaginary saddle would give a growth rate of 27.42. At $Pe = 50$ and $Ra = Ra_{\mathrm{a}}(50) \simeq 208.441$, the fit gives $(-2.5 \times 10^{-5}, 22.27621)$, against $(0, 22.27624)$ for the pair, although two imaginary saddles have positive rates 1.79 and 61.24. The differences from the pair predictions decrease when the fitting window is moved later. The direct signal thus supports the selected growth rates and frequencies in both cases, including neutrality at the threshold.

3.3 Uniqueness of the threshold

The selected pair defines a smooth growth function $g(r,p)$. Its derivatives are simple, because the derivative with respect to the saddle vanishes by stationarity:

$$g_r = \operatorname{Re} \frac{\kappa_*^2}{1+\kappa_*^2}, \qquad g_p = \operatorname{Im} \kappa_* = -\eta < 0. \tag{14}$$

The first sign is also fixed, $g_r > 0$. To see this, put $q = x_*^2 + \eta^2$ and $h = \eta^2$. Reality of r and p in the saddle condition gives

$$r = \frac{[(1+q)^2 - 4h]^2}{(1+q)^2 - 4qh}, \qquad p = \frac{8q\sqrt{h}\,(1+q-2h)}{(1+q)^2 - 4qh}. \tag{15}$$

If $g_r = 0$, then $2h = q(1+q)$; since $h < q$ this would imply $q < 1$, and substitution into (15) would give $r = (1-q^2)/(1+2q) < 1$, outside the domain. The sign is positive at $p = 0$ and hence everywhere.

Theorem 3 (Absolute threshold)**.** *For every $p > 0$ the equation $g(r,p) = 0$ has a unique solution $r_0(p) > 4$. It is analytic and strictly increasing,*

$$r_0'(p) = \frac{\eta}{g_r} > 0, \qquad Ra_{\mathrm{a}}(Pe) = \pi^2 r_0(Pe/\pi), \qquad Ra_{\mathrm{a}}(0) = 4\pi^2. \tag{16}$$

The first vertical mode becomes absolutely unstable before all others.

Proof. At $r = 4$ the temporal maximum is zero. Shifting the contour to $\kappa = \xi - \mathrm{i}\epsilon$, $\xi \in \mathbb{R}$, $0 < \epsilon < 1$, crosses no pole and gives $\operatorname{Re} L \le C\epsilon^2 - p\epsilon < 0$ with some constant C for small ϵ, so $g(4,p) < 0$. For fixed p and $r \to \infty$ the growth tends to infinity. Positivity of g_r gives existence and uniqueness of the zero, and simplicity of the saddle gives analyticity. For the vertical wavenumber $\gamma = m\pi$ the threshold is $Ra_{\mathrm{a},m} = \gamma^2 r_0(Pe/\gamma)$. On the neutral curve $r g_r = \operatorname{Re}(1+\kappa_*^2) + p\eta$, and (15) gives $\operatorname{Re}(1+\kappa_*^2) = 1 + q - 2h > 0$. Therefore

$$\frac{d}{d\gamma}\left[\gamma^2 r_0(Pe/\gamma)\right] = \gamma\,\frac{2\operatorname{Re}(1+\kappa_*^2) + p\eta}{g_r} > 0, \tag{17}$$

and the threshold increases strictly with the vertical mode number. □

3.4 The trailing edge stops

Theorem 3 makes the picture of section 2 precise. For $Ra > 4\pi^2$ the growth $g(r,p)$ is positive at $p = 0$, where it equals $r - 2\sqrt{r}$, and decreases strictly in p. It also tends to $-\infty$: shifting the Fourier contour to the line $\operatorname{Im}\kappa = -1/2$, which lies between the poles, gives $\operatorname{Re} L \le C(r) - p/2$ on that line with a constant $C(r)$, and hence $g(r,p) \le C(r) - p/2$. There is therefore a unique finite speed $c_*(Ra) > 0$, the linear spreading speed of the packet [37], such that

$$S(v) > 0 \quad \Longleftrightarrow \quad |Pe - v| < c_*(Ra). \tag{18}$$

The edges of the growing packet move with speeds $Pe \pm c_*$ (figure 2(b)), and the absolute threshold is the condition $Pe = c_*(Ra)$: the trailing edge stops.

The two conjugate contributions of the selected pair add up to a real oscillating response. On the absolute neutral curve its exponential rate vanishes, but its frequency is nonzero for $p > 0$. The edge of the packet is therefore stationary, while the crests keep moving. For a simple saddle the envelope of the critical signal decays as $t^{-1/2}$, and exponential growth starts above the threshold.

3.5 Why the saddle equations need a global selection

The neutral-saddle equations have several solutions. Published computations [12–14, 16, 17] decide among them by combining a smallest-threshold search with checks of contour admissibility, which identify the physical threshold at the parameter values checked. Theorem 2 makes these checks global. Figure 4 illustrates three distinct sources of ambiguity.

Unselected saddle heights (figure 4(a)). On the physical threshold the off-axis pair has $\operatorname{Re} L = 0$, whereas the upper imaginary saddle has $\operatorname{Re} L$ between 8 and 142 for $0.5 \le Pe \le 120$. At larger Pe the inner imaginary saddle also becomes positive. Both have zero index. Maximizing $\operatorname{Re} L$ over all algebraic saddles without checking their contributions would place the threshold too low.

Loss of the real-frequency condition under elimination (figure 4(b)). For $21.9 \lesssim Pe < 63.79$ the boundary polynomial $F = 0$ of section 4 has a real branch below the physical boundary on which the squared frequency $W = \Omega^2$ of the neutral wave $\Lambda = \mathrm{i}\Omega$ is negative. At $Pe = 50$ its root $Ra = 138.6$ ($r = 14.04$) is smaller than the threshold 208.44 ($r = 21.12$). This root is not a solution of the original neutral-saddle conditions with real frequency: it appears only after the frequency has been eliminated. The example concerns the algebraic route, which must be followed by frequency recovery and the condition $W > 0$.

Neutral imaginary saddles below the threshold (figure 4(c)). For anisotropic permeability, $a = 0.5$ and $Pe = 10$, the inner imaginary saddle $k = 1.66327\,\mathrm{i}$ is neutral at $R = 29.2327$, well below the physical threshold 41.17721566 (section 5.5). Celli and Barletta [17] display this solution in their figure 4 and reject it because the steepest-descent path crosses a singularity. Their admissibility check is essential here: a search for the smallest neutral value without it would return 29.2327. By theorem 2 the index of this saddle vanishes for all parameters, so the rejection holds globally.

4 The exact algebraic boundary

We now eliminate the frequency and obtain the exact curve in the plane of heating and throughflow. The selection theorem is needed before elimination: it tells which of several algebraic branches to keep.

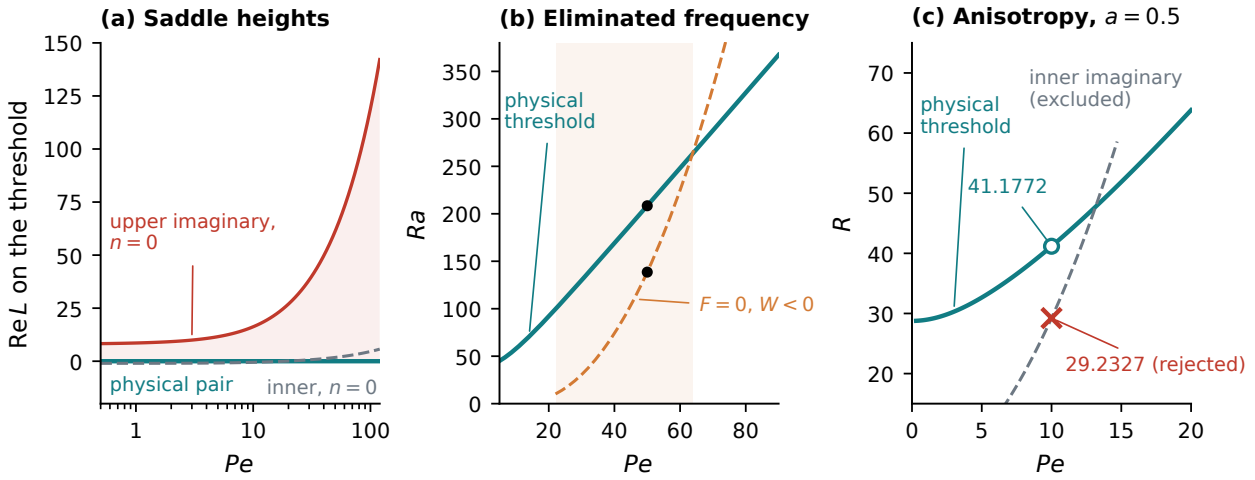


Figure 4: Three sources of ambiguity in saddle selection. (a) Growth $\mathrm{Re}\, L$ on the physical threshold: zero for the physical pair, positive for the upper and, at large Pe, the inner imaginary saddles, although their indices vanish. (b) A branch of the eliminated polynomial $F = 0$ of section 4 without real frequency ($W = \Omega^2 < 0$) lies below the physical boundary for $21.9 \lesssim Pe < 63.79$; the dots mark $Pe = 50$. (c) Anisotropy, $a = 0.5$: physical threshold and the neutral curve of the excluded inner imaginary saddle; the cross marks the neutral value $R = 29.2327$ of this saddle, shown and rejected in figure 4 of [17]; the circle is the threshold from (29). The figure was drawn with the AI-assisted Python code described under Computational methods.

4.1 The spurious stationary parabola

Let $\Delta(\Lambda)$ be the discriminant of the spatial quartic D with respect to κ. At zero frequency

$$\Delta(0) = (p^2 - 4r)^2\,[4p^2 + (r-4)^2]. \tag{19}$$

For $p > 0$ the stationary neutral branch is

$$r = \frac{p^2}{4}, \qquad Ra = \frac{Pe^2}{4}, \tag{20}$$

and there $D(\kappa, 0) = \left(\kappa^2 + \frac{\mathrm{i}p}{2}\kappa + 1\right)^2$. The square factor confirms that both spatial roots are double. Both saddles, however, are imaginary, $\kappa = \mathrm{i}\left[-p \pm \sqrt{p^2+16}\right]/4$. For $p > 2$ they are the inner and the lower outer saddles of theorem 2, both of zero index; for $p \le 2$ the branch lies in $r \le 1$, where the real-contour estimate already excludes absolute growth. The parabola is therefore not an absolute-instability boundary. Its discovery and exclusion are due to [12, 13]. The global selection establishes it together with the classification of all other saddles for all parameters.

4.2 The oscillatory boundary and frequency recovery

On the physical neutral curve put $\Lambda = \mathrm{i}\Omega$, $P = p^2/4$, $W = \Omega^2$. The real and imaginary parts of $\Delta(\mathrm{i}\Omega) = 0$ give two quadratic polynomials $\mathcal{U}(W)$, $\mathcal{V}(W)$, whose resultant is

$$\mathrm{Res}_W(\mathcal{U}, \mathcal{V}) = -r^2(r-P)F(r,P). \tag{21}$$

The polynomial F, given explicitly in appendix A, equation (65), has degree seven in r and five in P. The extra factor $r - P$ reproduces the spurious parabola. The equation $F = 0$ still contains

more than the physical threshold, because eliminating the squared frequency loses the condition $W > 0$ (figure 3(c)). The exact physical boundary is therefore

$$F(r, P) = 0, \quad r > 4, \quad \mathcal{U}(W) = \mathcal{V}(W) = 0 \text{ for some } W > 0, \tag{22}$$

with $\mathcal{U}$, $\mathcal{V}$ and the formula that recovers W also given in appendix A. A positive W restores a real nonzero frequency. The corresponding saddle cannot be imaginary and hence belongs to the unique physical pair, and theorem 3 guarantees uniqueness of the remaining solution. At $Pe = 50$, for example, F has two positive roots with $r > 4$:

r	W	meaning
14.0398794	−2506.1450	no real frequency
21.1194932	496.2309	$Ra_{\mathrm{a}} = 208.4410434$

The smaller root has no real frequency and is removed by frequency recovery. Choosing the saddle with the largest real part without checking its index would also give a wrong threshold (section 3.5).

4.3 The exact crossing and the projection node

The crossing of the physical boundary with the spurious parabola follows without continuation from

$$F(r, r) = r(r + 4)^4(8r^2 - 71r + 4). \tag{23}$$

The only admissible root gives

$$P_\times = r_\times = \frac{71 + 17\sqrt{17}}{16}, \qquad Pe_\times = \frac{\pi}{2}\sqrt{71 + 17\sqrt{17}} = 18.6583\ldots. \tag{24}$$

The numerical value of the crossing is known from previous work [12–14]. The factorization (23) gives its exact form. At this point one pair of physical parameters admits both an oscillatory neutral state and a non-pinching stationary double root, a feature of the projection that leaves the instability mechanism unchanged.

The plane curve $F = 0$ also has a node (figure 3(d)),

$$(r, P) = (26.65607919,\ 103.06526584), \qquad (Pe, Ra) = (63.78756623,\ 263.08495654). \tag{25}$$

The two branches give $W = -5951.9202584$ and 828.8568641 at the node. Only the latter represents a neutral oscillation. The physical boundary passes smoothly through the node, as theorem 3 requires. Frequency recovery thus separates a singularity of the projection from a physical encounter of modes.

5 One growth function for porous convection

In all generalizations considered here the buoyant response remains rational. Only the position of the poles and the neutral level of the selected saddle change.

5.1 General scaling

Consider the symbol

$$\lambda(k) = \mathcal{R}\frac{k^2}{A\pi^2 + Bk^2} - (k^2 + \pi^2) - \mathrm{i}\mathcal{P}k, \qquad A, B > 0, \tag{26}$$

where $\mathcal{R}$ measures buoyancy and $\mathcal{P}$ horizontal advection. With

$$\alpha = \pi\sqrt{A/B}, \qquad \kappa = k/\alpha, \qquad r = \mathcal{R}/(A\pi^2), \qquad p = \mathcal{P}/\alpha$$

one finds

$$\frac{\lambda}{\alpha^2} = L(\kappa; r, p) - s, \qquad s = \frac{B}{A} - 1 > -1. \tag{27}$$

The absolute growth rate in the original time scale is $\alpha^2[g(r,p) - s]$. A constant shift changes neither the saddles nor their ascending cycles, so the selection theorem transfers to this family and neutrality is $g = s$.

Proposition 4 (Threshold at a shifted level)**.** *For every $s > -1$ and $p \geq 0$ the equation $g(r,p) = s$ has a unique solution $r_s(p) > 1$. For $p > 0$*

$$\frac{\partial r_s}{\partial p} = \frac{\eta}{g_r} > 0, \qquad \frac{\partial r_s}{\partial s} = \frac{1}{g_r} > 0, \qquad r_s(0) = \bigl(1 + \sqrt{1+s}\bigr)^2. \tag{28}$$

Consequently

$$\mathcal{R}_{\mathrm{a}}(\mathcal{P}; A, B) = A\pi^2\, r_{B/A-1}\left(\frac{\mathcal{P}}{\pi\sqrt{A/B}}\right). \tag{29}$$

Proof. On the real contour $\operatorname{Re} L(\kappa; r, p) = r\kappa^2/(1+\kappa^2) - (1+\kappa^2) \leq r - 2\sqrt{r}$ for $r > 1$, and the Green function is bounded by the integral of $e^{t\operatorname{Re} L}$ along this contour. Hence

$$g(r,p) \leq r - 2\sqrt{r} \longrightarrow -1 \qquad (r \downarrow 1),$$

so $g < s$ near $r = 1$ for every $s > -1$; as $r \to \infty$ the growth tends to infinity. Positivity of g_r gives a single crossing of every level $s > -1$. The derivatives follow from implicit differentiation; at $p = 0$ one solves $r - 2\sqrt{r} = s$. □

For the vertical mode m,

$$\mathcal{R}_{\mathrm{a},m}(\mathcal{P}) = m^2\mathcal{R}_{\mathrm{a},1}(\mathcal{P}/m), \tag{30}$$

so the whole sequence of vertical thresholds is expressed through one curve.

Physically, the class comes from the linearized drag. Consider transverse-roll disturbances, whose roll axes are perpendicular to the basic flow, of a uniform throughflow $U\mathbf{e}_x$ with $U = Pe > 0$ in the units of section 2, under an instantaneous isotropic drag law $d(|\mathbf{u}|)\,\mathbf{u}$. Linearization gives the drag tensor $d_\perp I + (d_\parallel - d_\perp)\,\mathbf{e}_x\mathbf{e}_x^{\mathsf{T}}$ with $d_\perp = d(U)$ and $d_\parallel = d(U) + U\,d'(U)$. A disturbance along the flow changes both the speed and the drag coefficient, whereas one across the flow only turns the velocity. These disturbances obey the symbol (26) with $A = d_\parallel$ and $B = d_\perp$, up to a common factor absorbed into $\mathcal{R}$. Forchheimer drag, $d = 1 + Fo\,|\mathbf{u}|$ with the Forchheimer number Fo, gives $A = 1 + 2q$ and $B = 1 + q$, where $q = Fo\,U$. A power-law fluid with index ν, $d \propto |\mathbf{u}|^{\nu-1}$, gives $A = \nu$ and $B = 1$ after the common factor $d(U)$ is absorbed into $\mathcal{R}$. Anisotropic permeability gives $B/A = K_h/K_z$ directly. Every instantaneous isotropic drag law with $d_\parallel, d_\perp > 0$ thus leads to a level of the same growth function, while the open upper boundary changes the admissible

vertical wavenumbers. The statement concerns the linearized problem for these disturbances, not the nonlinear models.

The level also has a direct mechanical meaning:

$$1 + s = \frac{d(U)}{[U\, d(U)]'}, \qquad s = -\frac{U\, d'(U)}{d(U) + U\, d'(U)}.$$

The numerator in the first ratio is the secant resistance of the pressure–flow curve, and the denominator is its tangent resistance. Thus $d_{\parallel} > 0$ expresses local monotonicity of this curve. Equivalently, its local logarithmic slope $\nu_{\mathrm{eff}} = \mathrm{d}\log[U\, d(U)]/\mathrm{d}\log U$ gives $s = \nu_{\mathrm{eff}}^{-1} - 1$. Under the assumed positive resistances, decreasing $d(U)$ gives $s > 0$, while increasing $d(U)$ gives $s < 0$. The physical threshold also depends on the resistance scale and on the rescaled advection parameter.

Interphase heat exchange. The same level construction applies to a thermal sink. In the high-conductivity limit for the solid matrix of Freitas *et al.* [21, Eq. (16)], the dispersion relation for rolls uniform in the spanwise direction is, with $\mu_m = m\pi$,

$$\lambda_m(k) = R\frac{k^2}{k^2 + \mu_m^2} - (k^2 + \mu_m^2) - H - \mathrm{i}Pek.$$

The heat exchange term $-H$ shifts the growth rate without changing the saddle locations or the contours at fixed R and Pe. Hence

$$R_{\mathrm{a},m}(Pe, H) = \mu_m^2 r_{H/\mu_m^2}(Pe/\mu_m), \qquad \left.\frac{\partial R_{\mathrm{a},m}}{\partial H}\right|_{Pe,m} = \frac{1}{g_r} > 0$$

by proposition 4. At $Pe = 10$ and $H = 30$, this gives $R_{\mathrm{a},1} = 102.28205$, within 6×10^{-5} of the value 102.2820 reported for the spanwise-uniform mode in figure 8 of [21].

5.2 The universality map

Thresholds can then be computed without any search over complex wavenumbers.

Algorithm 1. *Absolute threshold of the first vertical mode for any model of the form* (26).

1. From the model parameters form A, B and $\mathcal{P}$; set $s = B/A - 1$ and $p = \mathcal{P}/(\pi\sqrt{A/B})$.
2. Bracket the root: by proposition 4, $g(r, p) - s < 0$ as $r \to 1^+$ and $g \to \infty$ as $r \to \infty$; start from $r_{\mathrm{hi}} = 8$ or any larger value and double r_{hi} until $g(r_{\mathrm{hi}}, p) > s$.
3. Solve $g(r, p) = s$ on $(1, r_{\mathrm{hi}})$ by a bracketing root finder, which keeps a sign change while shrinking the interval: bisection, or Brent's method [38], used in the implementation. Each evaluation of g takes the off-axis root of the quintic (8) with positive real part. By proposition 4 the root is unique.
4. Return $\mathcal{R}_{\mathrm{a}} = A\pi^2 r_s(p)$, or use the explicit parametrization of section 5.8 instead of steps 2–3.

Other vertical modes follow from (30). The selection is done once by theorem 2, so a single scalar equation with a guaranteed bracket replaces the three real nonlinear equations solved at each parameter point.

Figure 5(a) shows $r_s(p)$ on the plane (p, s) with representative model trajectories. The Prats problem and the layer with an open upper boundary lie on $s = 0$. Forchheimer drag with $q = Fo\, Pe$ (Forchheimer number Fo, section 5.3) moves from $s = 0$ towards $s = -1/2$. Transverse rolls of a power-law fluid with index ν and anisotropic permeability with ratio $a = K_h/K_z$ (sections 5.4

and 5.5) give the horizontal levels $s = 1/\nu - 1$ and $s = a - 1$. Coincidences of levels are immediate: a power-law fluid with $\nu = 2$ and anisotropy with $a = 1/2$ share $s = -1/2$, and $\nu = 1/2$ and $a = 2$ share $s = 1$. Their thresholds differ only by the scales in (29). A vertical magnetic field with resistance factor M gives the level $s = 1/M - 1$ (section 5.7). Figure 5(b) tests the tabulated transverse-mode benchmarks, mapped to (r, p, s) and inserted in g. The tabulated magnetic and zero-field thresholds agree with the calculation to better than 10^{-6} relative error. The Forchheimer thresholds quoted as integers by Delache *et al.* agree to within 0.5%, two of the three to their quoted precision. The rejected imaginary-saddle value 29.2327 shown in figure 4 of [17] falls off the diagonal, $g = -1.151$ at $s = -1/2$.

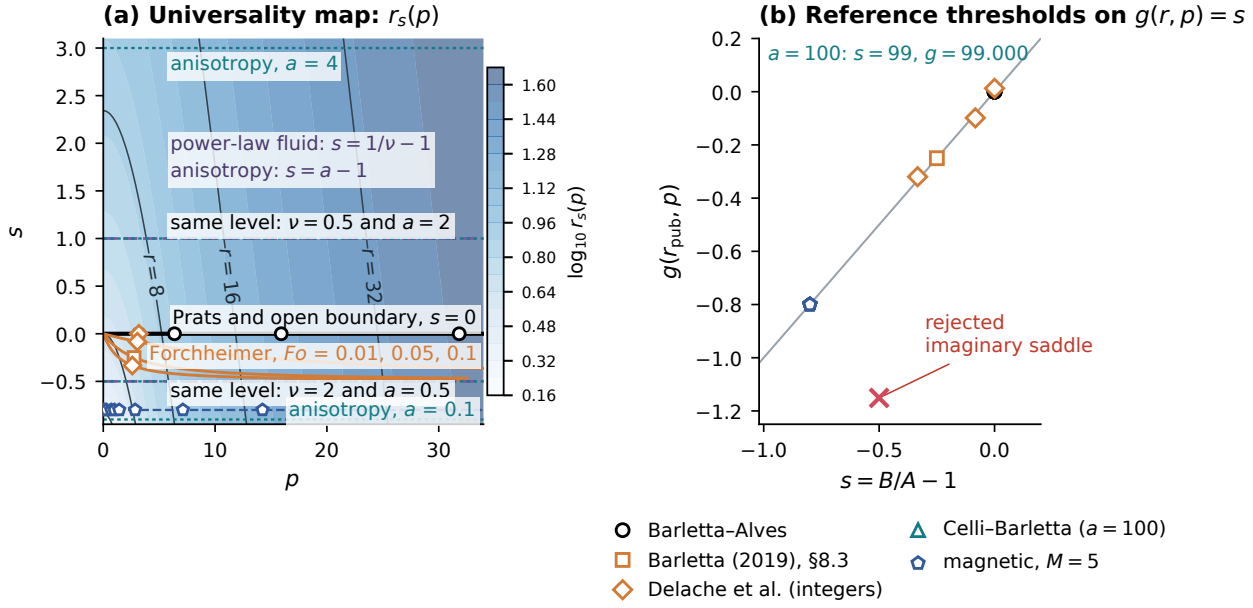


Figure 5: Universality. (a) The threshold $r_s(p)$ on the plane (p, s) (color and contours) with the model trajectories: Prats and open boundary ($s = 0$), Forchheimer drag with $q = Fo\,Pe$, $Fo = 0.01$, 0.05, 0.1, power-law fluid ($s = 1/\nu - 1$) and anisotropy ($s = a - 1$), and magnetic resistance ($M = 5$, $s = -0.8$); markers are tabulated values. (b) Reference thresholds mapped to (r, p, s) by (29): Barletta and Alves [12], the monograph [14] (§8.3), Delache *et al.* [8] (integers quoted in their section 4.1) and Celli and Barletta [17] ($a = 100$, $s = 99$, given as a number), and the magnetic case $M = 5$ of Turkyilmazoglu [15]. The cross is the neutral value 29.2327 of the inner imaginary saddle, shown and rejected in figure 4 of [17]. The figure was drawn with the AI-assisted Python code described under Computational methods.

5.3 Forchheimer drag

In the model of Delache *et al.* [8] the inertial drag is characterized by $q = Re_K = Fo\,Pe$, where Fo is the Forchheimer number (denoted F in [8]). For transverse rolls their dispersion relation (equation (9) of [8] with $m = 0$) has the buoyant denominator $(1+2q)\pi^2 + (1+q)k^2$, so $A = 1+2q$, $B = 1+q$, $s = -q/(1+2q)$ and

$$Ra_{\mathrm{a}} = \pi^2 (1+2q)\, r_{-q/(1+2q)} \left(\frac{Pe}{\pi} \sqrt{\frac{1+q}{1+2q}} \right). \tag{31}$$

Under a change of observer only Pe in the argument is replaced by $|Pe - v|$. The drag parameter q is set by the basic flow and stays fixed. The temporal threshold is

$$Ra_T = \pi^2\bigl(\sqrt{1+2q} + \sqrt{1+q}\bigr)^2. \tag{32}$$

At $Pe = 10$ formula (31) gives 57.80, 66.29 and 141.31 for $Fo = 0$, 0.01, 0.1. Delache *et al.* quote these thresholds as the integers 58, 66 and 142 (section 4.1 of [8]; also p. 56 of [9]). The first two agree after rounding to the nearest integer, while 142 exceeds 141.31 by 0.49%, a difference whose origin cannot be determined from the paper. For Barletta's form-drag parameter $G = 0.05$ at $Pe = 10$, that is $q = GPe = 0.5$, formula (31) gives 99.7984, the value in equation (8.69) of [14].

5.4 Transverse rolls of a power-law fluid

In the setting of Alves and Barletta [16] let $\nu > 0$ be the power-law index. For transverse rolls $\mathcal{R} = R/Pe^{\nu-1}$, where R is their Darcy–Rayleigh number, and $A = \nu$, $B = 1$; hence

$$R_{\mathrm{a}} = \nu\pi^2 Pe^{\nu-1}\, r_{(1-\nu)/\nu}\!\left(\frac{Pe}{\pi\sqrt{\nu}}\right), \qquad R_T = \pi^2 Pe^{\nu-1}(1+\sqrt{\nu})^2. \tag{33}$$

These formulas describe the family of transverse disturbances. The competition with longitudinal and oblique rolls studied in [16] requires a comparison of the corresponding families and is outside the present class. Within the transverse problem the whole complex selection is already done by theorem 2.

5.5 Anisotropic permeability

Let $a = K_h/K_z$ be the ratio of horizontal to vertical permeability. In the normalization of Celli and Barletta [17] the Rayleigh number is built on K_h, and $A = 1$, $B = a$, $s = a - 1$. Therefore

$$R_{\mathrm{a}} = \pi^2\, r_{a-1}\!\left(\frac{Pe\sqrt{a}}{\pi}\right). \tag{34}$$

Increasing a raises both the argument and the level, and both sensitivities in (28) are positive:

$$\frac{\partial R_{\mathrm{a}}}{\partial Pe} = \frac{\pi\sqrt{a}\,\eta}{g_r} > 0, \qquad \frac{\partial R_{\mathrm{a}}}{\partial a} = \frac{\pi^2}{g_r}\left(1 + \frac{Pe\,\eta}{2\pi\sqrt{a}}\right) > 0. \tag{35}$$

The monotonicities found numerically in [17] are thus confirmed analytically. At $a = 100$, $Pe = 10$ one obtains the published threshold 1545.47; at $a = 0.5$, $Pe = 10$ the threshold is 41.1772 (section 3.5). At $Pe = 0$, $R_{\mathrm{a}} = \pi^2(1+\sqrt{a})^2$, and for fixed Pe and $a \to 0$, $R_{\mathrm{a}} \to \pi^2$, as found in [17]. The last limit needs no expansion near the degenerate level $s = -1$: for every fixed $r > 1$, $g(r, 0) = -1 + (\sqrt{r} - 1)^2 > -1$, so for small a the threshold lies between 1 and any such r. Figure 6 compares anisotropy with inertial drag in physical variables.

5.6 An open upper boundary

In the problem of Barletta and Celli [13] the vertical wavenumbers are $(m - \frac{1}{2})\pi$. For the first mode

$$Ra_{\mathrm{a}}^{\mathrm{BC}}(Pe) = \tfrac{1}{4} Ra_{\mathrm{a}}(2Pe), \tag{36}$$

an equivalence already stated in their equation (35). Together with the selection theorem it transfers the whole exact boundary, the expansions and the convergence certificates to the open layer. Both radii in the variable Pe are halved.

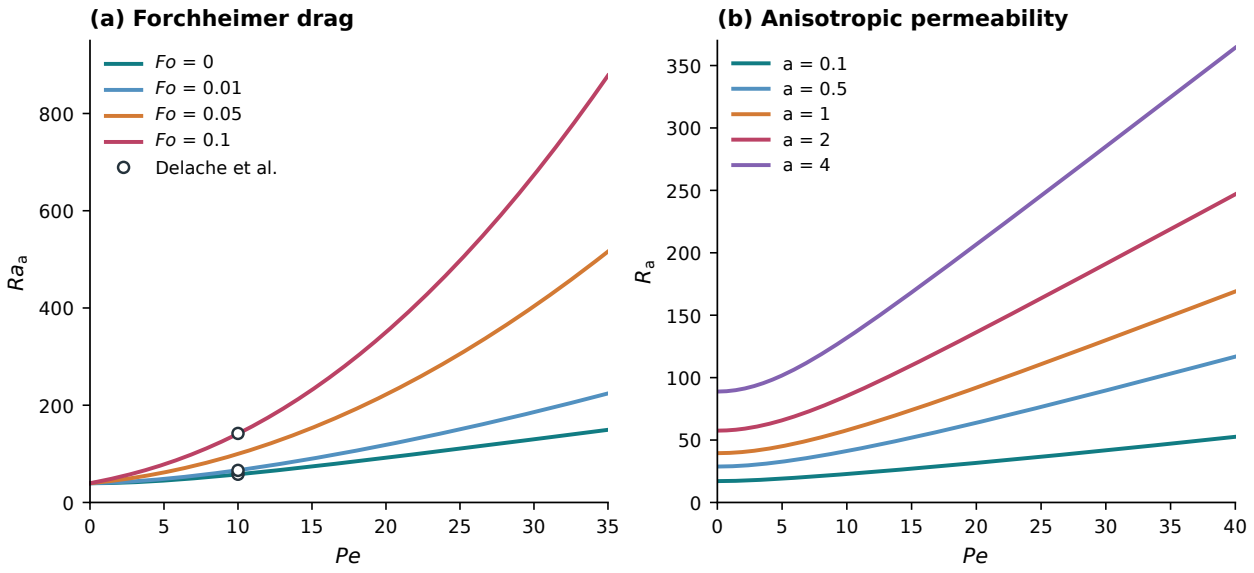


Figure 6: Two applications in physical variables. (a) Forchheimer drag with $q = Fo\,Pe$; markers are rounded published values at $Pe = 10$. (b) Anisotropic permeability for several $a = K_h/K_z$. All curves follow from (29) without any optimization over the complex wavenumber. The figure was drawn with the AI-assisted Python code described under Computational methods.

5.7 A vertical magnetic field

Capone and Rionero [39] found magnetic stabilization in a modal and energy stability analysis of porous convection. Here the threshold of interest is absolute instability at prescribed horizontal throughflow. In Turkyilmazoglu's Darcy model, the Lorentz force adds a dimensionless resistance $Q \geq 0$ to the horizontal resistance and leaves the vertical resistance unchanged. His dispersion relation for transverse rolls [15, Eq. (12)] has the form (26) with $A = M = 1 + Q$, $B = 1$, $\mathcal{R} = Ra$ and $\mathcal{P} = Pe$. Hence the first-mode threshold is

$$Ra_{\mathrm{a}}(Pe, Q) = M\pi^2 r_{1/M-1}\left(\frac{Pe}{\pi\sqrt{M}}\right).$$

Tables 1 and 2 of [15] give 19 finite-Pe benchmarks at zero field and $M = 5$. For example, at $Pe = 10$ the calculation gives $Ra_{\mathrm{a}} = 57.80357$ for $M = 1$ and 142.34085 for $M = 5$. The leading large-Pe term $c_1\sqrt{M}\,Pe$ and the limiting saddle $k_\infty = \pi\sqrt{M}\,\kappa_\infty$ agree with Eq. (24) of [15]; the second term follows from the general expansion in section 6.5.

Monotonicity at prescribed throughflow. For the entire class (26), $\mathcal{R}_{\mathrm{a}}(\mathcal{P}; A, B)$ increases strictly with either A or B when the other coefficient and $\mathcal{P}$ are held fixed. In particular, increasing Q at fixed Pe raises the absolute threshold.

Proof. It suffices by reflection to take $\mathcal{P} > 0$. Let $w = \kappa_*^2$ at the selected saddle on the threshold. The contribution from the motion of the saddle vanishes upon differentiating $\mathrm{Re}\,\lambda(k_*) = 0$, since $\lambda_k(k_*) = 0$. At fixed throughflow the derivatives are therefore

$$\frac{A}{\mathcal{R}_{\mathrm{a}}}\,\partial_A\mathcal{R}_{\mathrm{a}} = \frac{\mathrm{Re}[w/(1+w)^2]}{g_r}, \qquad \frac{B}{\mathcal{R}_{\mathrm{a}}}\,\partial_B\mathcal{R}_{\mathrm{a}} = \frac{\mathrm{Re}[(w/(1+w))^2]}{g_r}, \qquad g_r = \mathrm{Re}\,\frac{w}{1+w} > 0.$$

To determine the signs, put $q = |w|$, $\delta = \operatorname{Re} w$ and $\eta = -\operatorname{Im}\kappa_* > 0$. The stationarity identities (15) read

$$D_q = 1 + 2q(1+\delta) - q^2, \qquad r = \frac{(1+2\delta+q^2)^2}{D_q}, \qquad p = \frac{8\eta q(1+\delta)}{D_q}.$$

Since $r, p > 0$, $D_q > 0$ and $\delta > -1$. Neutrality, $rg_r - \delta - p\eta = B/A$, then gives

$$\frac{B}{A} D_q = q^4 - 3q^2 + 2(1+q)\delta^2 + 2q\delta.$$

For $0 < q < 1$, the right-hand side is a convex quadratic in δ. Its values at $\delta = -q$ and $\delta = 0$ are $q^2(q-1)(q+3)$ and $q^2(q^2-3)$, respectively, so it is negative throughout $[-q, 0]$. Neutrality therefore requires $\delta > 0$ for $q < 1$. Now $|1+w|^4 \operatorname{Re}[w/(1+w)^2] = (1+q^2)\delta + 2q^2$. This is positive for $q < 1$ and exceeds $q^2 - 1$ for $q \geq 1$ since $\delta > -1$. For the other derivative, stationarity gives $rw/(1+w)^2 = w + \mathrm{i}p\kappa_*/2$. Subtracting its real part, $\delta + p\eta/2$, from rg_r and using neutrality gives $r \operatorname{Re}[(w/(1+w))^2] = B/A + p\eta/2 > 0$. At $\mathcal{P} = 0$, $\mathcal{R}_\mathrm{a} = \pi^2(\sqrt{A} + \sqrt{B})^2$, which has the same strict monotonicities. □

Figure 6(d) of Turkyilmazoglu [15] compares thresholds for different M by plotting Ra_a against $\operatorname{Im} k_*$. The curves cross in this plot, where points at the same $\operatorname{Im} k_*$ generally have different imposed throughflows. At $\operatorname{Im} k_* = -3.2$, for example, the pairs (Pe, Ra_a) are approximately $(87.96, 359.19)$ at $M = 1$ and $(12.93, 160.18)$ at $M = 5$. The lower threshold in the second pair does not describe a change of magnetic field alone. At fixed Pe the order is instead fixed by the monotonicity just proved.

5.8 Explicit parametrization of every level

Write $q = |\kappa_*|^2$, $h = (\operatorname{Im}\kappa_*)^2$ and $B_q = (1+q)^2 - 4qh$. Substituting (15) into $g(r,p) = s$ gives a quadratic in h:

$$N_s(q,h) = 8(q+1)h^2 - 4q(2q - s + 2)h + q^4 + 2q^3 - sq^2 - 2sq - 2q - s - 1 = 0. \tag{37}$$

This is the neutral-saddle equation of Turkyilmazoglu [15, Eq. (18)] in different variables. For $k = k_r + \mathrm{i}k_i$, substituting $k_r^2 = M\pi^2(q-h)$, $k_i^2 = M\pi^2 h$ and $s = 1/M - 1$ gives his numerator as $(M\pi^2)^4 N_s(q,h)$. His radical parametrization uses k_i and covers the Prats and magnetic cases, $-1 < s \leq 0$. The quadratic form uses q and works for every $s > -1$, with the contributing saddle specified by theorem 2. The two roots at fixed q are

$$h(q) = \frac{q(2q - s + 2) \pm \sqrt{-T_s(q)}}{4(q+1)}, \tag{38}$$

with

$$T_s(q) = 2q^5 + 2q^4 + (2s-4)q^3 - (s^2 + 2s + 8)q^2 - 6(s+1)q - 2(s+1). \tag{39}$$

Once h is chosen, heating, throughflow and the angular frequency Ω (in canonical units, with the phase convention $e^{\lambda t + \mathrm{i}kx}$) follow:

$$r = \frac{[(1+q)^2 - 4h]^2}{B_q}, \qquad p = \frac{8q\sqrt{h}\,(1+q-2h)}{B_q}, \qquad \Omega = -\frac{8\sqrt{h}\,(1+q)(q-h)^{3/2}}{B_q}. \tag{40}$$

The physical arc starts at $q = \sqrt{1+s}$, $h = 0$ and is continued with $0 < h < q$, $B_q > 0$ and $p > 0$. The sign of the radical in (38) changes where the two branches meet, at a zero of T_s. The selection theorem guarantees that every p corresponds to exactly one point of this arc. For a fixed anisotropy ratio this gives the curves of figure 6(b) directly, since the level $s = a - 1$ is constant along each of them. For the saddle with positive real part $\Omega < 0$, so the phase moves downstream.

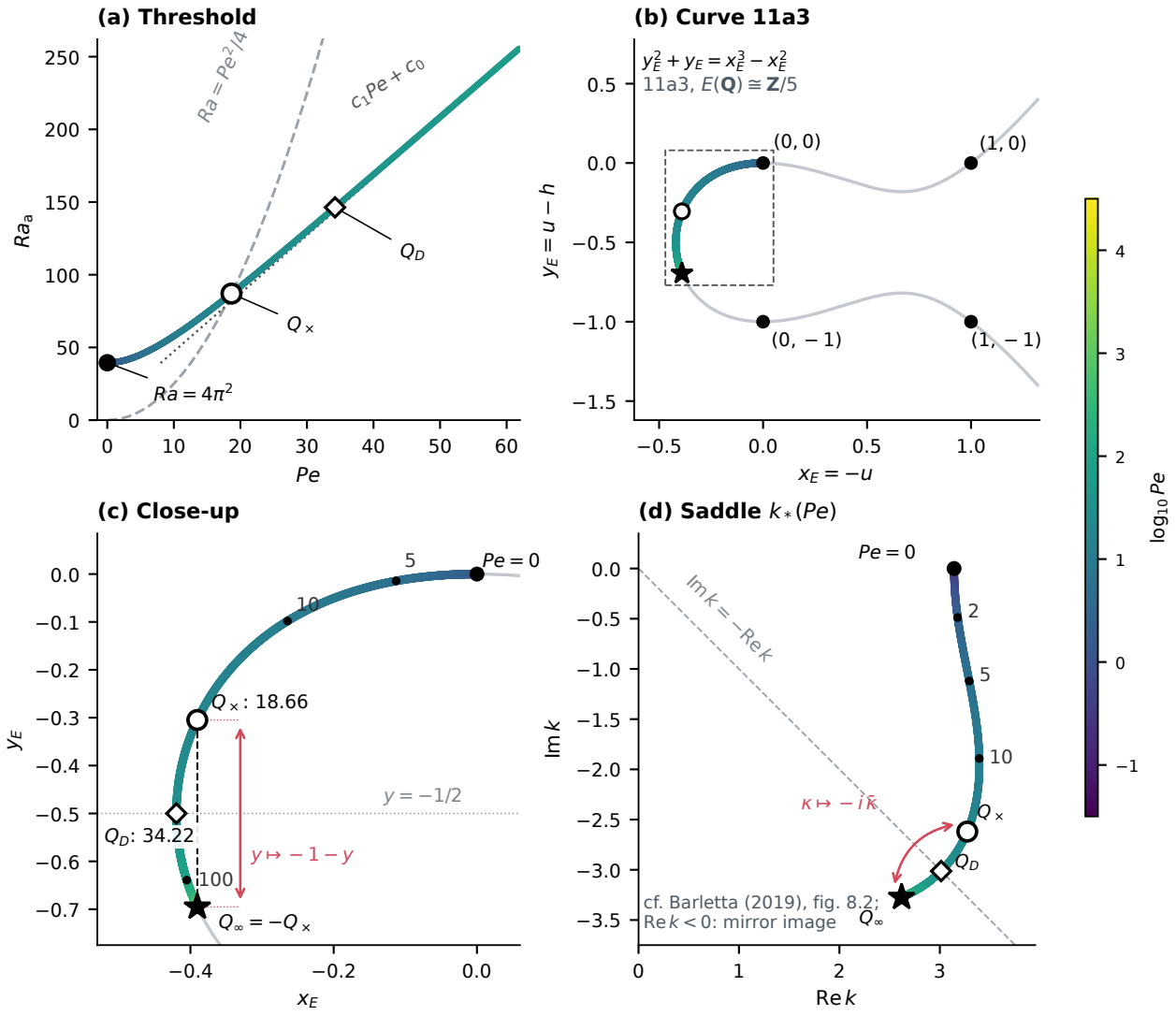


Figure 7: One physical arc in four charts. (a) Threshold $Ra_a(Pe)$ and its crossing $Q_\times$ with the parabola $Ra = Pe^2/4$ at $Pe = 18.658$; the dotted line is the two-term asymptote $c_1 Pe + c_0$ of (54). (b) The curve 11a3, a model of the modular curve $X_1(11)$, with its rational points and the physical arc, colored by $\log_{10} Pe$; the four marked rational points and $\mathcal{O}$ at infinity form $E(\mathbb{Q}) \cong \mathbb{Z}/5$ [40]. (c) Close-up of the arc: $Q_\times$ and the limit point Q_∞ ($Pe \to \infty$) are opposite in the group law. The point Q_D ($Pe = 34.22$) is the vertical tangent of the elliptic curve; the physical threshold in (a) is smooth there. (d) The same arc in the chart $k = \pi\kappa$, that is, the trajectory of $k_* = \pi\kappa_*$, comparable with figure 8.2 of [14]. The reflection $y_E \mapsto -1 - y_E$ corresponds to $\kappa \mapsto -\mathrm{i}\bar{\kappa}$ in the diagonal $\mathrm{Im}\, k = -\mathrm{Re}\, k$. The figure was drawn with the AI-assisted Python code described under Computational methods.

6 Elliptic geometry and expansions of the threshold

The physical boundary is one arc of a known elliptic curve (figure 7(a,b)). Parametrizing this arc computes the threshold across the whole range of throughflow, and its two end points generate two different convergent series.

6.1 One arc instead of saddle continuation

For $s = 0$ replace q by $1 + 2u$. After removing the factor $q + 1$, equation (37) becomes

$$E(u, h) = h^2 - (1 + 2u)h + u(1 + u)^2 = 0. \tag{41}$$

Equation (41) describes the off-axis oscillatory neutral locus. Its physical arc gives the absolute-instability threshold. The stationary imaginary saddles form the separate parabola (20).

With $\mathcal{A} = (1 + u)^2 - h$, $\mathcal{B} = (1 + u)^2 - (1 + 2u)h$ and $\mathcal{C} = (1 + 2u)^2 h(1 + u - h)^2$,

$$r = \frac{4\mathcal{A}^2}{\mathcal{B}}, \qquad P = \frac{4\mathcal{C}}{\mathcal{B}^2}, \qquad Pe = 2\pi\sqrt{P}, \qquad Ra = \pi^2 r, \tag{42}$$

and h is found from one square root,

$$h_\pm(u) = \frac{1 + 2u \pm \sqrt{1 - 4u^2 - 4u^3}}{2}. \tag{43}$$

The full route has two parts. First take h_- and increase u from zero to the positive root of $4u_D^3 + 4u_D^2 - 1 = 0$, $u_D = 0.419643\ldots$; then take h_+ and decrease u to

$$u_\infty = \frac{\sqrt{17} - 1}{8}, \qquad h_\infty = \frac{5 + 3\sqrt{17}}{16}. \tag{44}$$

At the start $Pe = 0$ and $Ra = 4\pi^2$; at the end $\mathcal{B} \to 0^+$ and $Pe \to \infty$. The change of sign of the radical occurs at $Pe \simeq 34.216$, where the physical threshold remains smooth. The whole range of throughflows is thus computed without an initial guess for a complex root.

The change of coordinates $x_E = -u$, $y_E = u - h$ brings (41) to

$$y_E^2 + y_E = x_E^3 - x_E^2, \tag{45}$$

the curve 11a3 in Cremona's notation (11.a3 in the LMFDB [40]), with discriminant -11 and j-invariant $-4096/11$. It is a model of the modular curve $X_1(11)$ [40]. In the variables $q = |\kappa|^2$, $h = (\operatorname{Im}\kappa)^2$ equation (41) is the polar curve $|\kappa|^6 + |\kappa|^4 \cos 4\varphi - |\kappa|^2 = 1$, $\varphi = \arg\kappa$. Barletta and Celli [13] use it to describe the off-axis part of the set of neutral saddles; the rest of that set is the imaginary axis. The physical arc is the saddle trajectory drawn in figure 8.2 of [14]; Turkyilmazoglu [15] also parametrizes the nonmagnetic locus in radicals. In the present description r and P are rational functions of the coordinates of the elliptic model. The two square-root branches describe one selected arc, including its passage through the turning point of the coordinate u.

The crossing with the spurious parabola has the same $u = u_\infty$ but

$$h_\times = \frac{7 + \sqrt{17}}{16}, \qquad y_{E,\times} + y_{E,\infty} = -1, \tag{46}$$

so on (45) the two points are opposite in the group law. Their complex wavenumbers satisfy $\kappa_\times = -\mathrm{i}\,\overline{\kappa_\infty}$: in the saddle chart the negation is the reflection in the diagonal $\operatorname{Im} k = -\operatorname{Re} k$, and the point Q_D where the radical changes sign is its fixed point (figure 7c,d). This symmetry links the finite crossing with the limit of strong throughflow and explains why $\sqrt{17}$ appears in both.

6.2 Why a general level has genus two

Completing the square in (37) gives

$$y^2 = -T_s(q), \qquad y = 4(q+1)h - q(2q - s + 2). \tag{47}$$

The discriminant of the quintic is

$$\operatorname{Disc}_q T_s = 16s^4(s+1)(s^2+3s+88)(54s^4+239s^3+384s^2-80s+64). \tag{48}$$

The last two factors are positive on the real axis. For the quartic this is seen directly: for $s \geq 0$ the part $384s^2 - 80s + 64$ is positive and the other terms are non-negative, while for $s < 0$ one has $s^2(54s^2+239s+384)-80s+64 > 0$, because the quadratic $54s^2+239s+384$ has negative discriminant and $-80s > 0$. In the physical domain $s > -1$ the quintic therefore has distinct roots for $s \neq 0$. The map $(q, y) \mapsto q$ from the curve $y^2 = -T_s(q)$ to the Riemann sphere has degree $n = 2$ and six simple branch points: the five roots of T_s and $q = \infty$, where the odd degree of T_s makes $y \sim q^{5/2}$ change sign around infinity. The Riemann–Hurwitz formula $2g-2 = n(2g_0-2)+\sum_p(e_p-1)$ [41], with genus $g_0 = 0$ of the sphere and ramification index $e_p = 2$ at each branch point, gives $2g - 2 = 2 \cdot (-2) + 6$, that is, genus $g = 2$. At $s = 0$ the polynomial (37) factorizes:

$$N_0 = (q+1)\big[8h^2 - 8qh + (q-1)(q+1)^2\big], \tag{49}$$

and the second factor is the elliptic curve (41). The elliptic case is a degeneration of a genus-two family, and the global selection applies beyond it. The group law, the rational torsion point at $Pe = 0$ and the elliptic inversion formula below are specific to $s = 0$, that is, to the Prats problem and the equivalent open-boundary problem.

6.3 Weak throughflow and integer coefficients

For a weak throughflow the threshold is naturally compared with $4\pi^2$. With $z = Pe^2/(16\pi^2)$ and $Y(z) = Ra_{\mathrm{a}}(Pe)/(4\pi^2)$,

$$Y(z) = 1 + z - z^2 + 3z^3 - 13z^4 + 68z^5 - 400z^6 + 2549z^7 - 17211z^8 + \cdots . \tag{50}$$

The leading shift $Ra_{\mathrm{a}} - 4\pi^2 \approx Pe^2/4$ follows from the Ginzburg–Landau approximation in Dufour and Néel [6, Sec. III B] and Chung *et al.* [7, Eqs. (21) and (22)]; see also [9, 24]. The exact expansion differs from this approximation starting at order Pe^4. Odd powers of Pe are absent because the threshold does not depend on the direction of the flow.

The coefficients follow directly from the boundary polynomial of appendix A. Since $r = 4Y$ and $P = 4z$, the threshold satisfies

$$F\big(4Y(z), 4z\big) = 0, \qquad Y(0) = 1.$$

Substituting $Y = 1 + Y_1 z + Y_2 z^2 + \cdots$ and equating the coefficients of equal powers of z gives, after division by $4F_r(4,0) = 200704$, where $F_r = \partial F/\partial r$, one linear equation for each new coefficient. With previously determined coefficients substituted at each step, the first three orders give $Y_1 = 1$, $Y_2 = -1$ and $Y_3 = 3$. In general, if $Y_1, \ldots, Y_{n-1}$ are known,

$$Y_n = -\frac{1}{200704}\,[z^n]\,F\Big(4\Big[1 + \sum_{j=1}^{n-1} Y_j z^j\Big],\, 4z\Big), \tag{51}$$

where $[z^n]$ denotes the coefficient of z^n in the polynomial that follows it. Because $F_r(4,0) = 50176 \neq 0$, every coefficient is determined uniquely. The recursion produces rational numbers; that they are integers is a separate statement.

Integrality of all coefficients is an exact property of this normalization. From (42), on the branch $u(0) = h(0) = 0$,

$$E(u, h) = 0, \qquad z\mathcal{B}^2 = \mathcal{C}, \qquad Y = \mathcal{A}^2/\mathcal{B}.$$

At $z = u = h = 0$ the Jacobian of the first two equations with respect to (u, h) is $\left(\begin{smallmatrix} 1 & -1 \\ 0 & -1 \end{smallmatrix}\right)$, with determinant -1. Determining the coefficients order by order, each step solves the same integer system with determinant -1, so $u, h \in \mathbb{Z}[[z]]$. The first terms are $u = z - 3z^2 + 14z^3 - 83z^4 + \cdots$ and $h = z - 2z^2 + 9z^3 - 54z^4 + \cdots$. Since $\mathcal{B}(0) = 1$, division preserves integrality, and

$$Y \in \mathbb{Z}[[z]]. \tag{52}$$

By Eisenstein's theorem [42] the coefficients of any algebraic series with rational coefficients become integral after a suitable integer rescaling of the argument and the value. Here the natural physical normalization already does this. At other rational levels with rational $\sqrt{1+s}$ a nontrivial rescaling may be needed. In practice any order of the small series follows from an exact integer recursion, without repeated differentiation of a complex saddle. Both recursions, (51) and the integer lifting of (u, h), are implemented in the script `prats_series.py`, which checks that they agree. At the time of writing, the OEIS contains no matching entry for the signed coefficients of (50) or their absolute values [43].

6.4 Strong throughflow

As $Pe \to \infty$ the physical saddle tends to

$$\kappa_\infty = \frac{\sqrt{7+\sqrt{17}}}{4} - \mathrm{i}\frac{\sqrt{5+3\sqrt{17}}}{4}, \tag{53}$$

a formula that, together with the leading coefficient c_1, is known from [13–15]. We continue the expansion in closed form,

$$Ra_\mathrm{a} = c_1 Pe + c_0 + \frac{c_{-1}}{Pe} + \frac{c_{-2}}{Pe^2} + O(Pe^{-3}), \tag{54}$$

with

$$\begin{aligned} c_1 &= \frac{\pi}{8}\sqrt{51\sqrt{17} - 107}, \qquad c_0 = \frac{\pi^2}{16}(49 - 9\sqrt{17}), \\ c_{-1} &= \frac{5\pi^2}{136}(17 + 7\sqrt{17})\, c_1, \qquad c_{-2} = \frac{3\pi^4(1445 + 163\sqrt{17})}{1156}. \end{aligned} \tag{55}$$

Numerically $c_1 = 3.990842\ldots$, $c_0 = 7.335613\ldots$, $c_{-1} = 66.411910\ldots$, $c_{-2} = 535.176892\ldots$. The constant correction was estimated by Richardson extrapolation in [18]. The coefficients beyond c_1 follow from a routine continuation of the leading balance of [13], and the inversion formula of section 6.6 gives them at every order. The linear law has a simple meaning in terms of the packet edges. At the threshold the flow speed equals the spreading speed, so $c_*(Ra) \sim Ra/c_1$: stronger heating lets the packet spread against a faster flow. The constant and the inverse powers are diffusive corrections to this balance. The four terms give relative errors 0.1542% at $Pe = 20$, 0.0101% at $Pe = 50$ and 0.000697% at $Pe = 100$.

6.5 A general two-term law

The same limiting saddle gives a compact formula for the whole class (26). For fixed A, B,

$$\mathcal{R}_\mathrm{a} = c_1\sqrt{AB}\,\mathcal{P} + \frac{\pi^2}{16}\big[(13 - 5\sqrt{17})A + 4(9 - \sqrt{17})B\big] + O(\mathcal{P}^{-1}). \tag{56}$$

It suffices to evaluate at the limiting saddle $\mathrm{Re}\,\frac{\kappa_\infty^2}{1+\kappa_\infty^2} = \frac{9+\sqrt{17}}{16}$ and $\mathrm{Re}(1+\kappa_\infty^2) = \frac{9-\sqrt{17}}{8}$; a change of level by s shifts the constant part of r_s by $s/g_r = (9-\sqrt{17})s/4$, and substitution of $s = B/A-1$ and the physical scales gives (56). The product AB sets the leading cost of holding the packet and the ratio A/B its spatial scale, $k_\infty = \pi\sqrt{A/B}\,\kappa_\infty$. For anisotropy $R_\mathrm{a} \sim c_1\sqrt{a}\,Pe$, for a power-law fluid $R_\mathrm{a} \sim c_1\sqrt{\nu}\,Pe^{\nu}$. In the Forchheimer model the coefficients grow with the flow: for fixed $Fo > 0$, $A \sim 2Fo\,Pe$, $B \sim Fo\,Pe$, $s \to -1/2$, and

$$Ra_\mathrm{a} \sim \sqrt{2}\,c_1 Fo\,Pe^2. \tag{57}$$

This quadratic law and its coefficient $5.64390\ldots$ are given in equation (8.75) of [14]. The growth function shows how the linear, power and quadratic laws arise from one saddle.

6.6 All orders of the large series

On the elliptic curve the large series can be inverted once to give a formula of any order. Put

$$X = \frac{c_1}{\pi}, \qquad \tau = \frac{\pi^2}{c_1 Pe} = \frac{1}{Xp}, \qquad \frac{Ra_\mathrm{a}}{c_1 Pe} = \sum_{n=0}^{\infty} b_n \tau^n, \qquad c_{1-n} = \pi^{2n} c_1^{1-n} b_n. \tag{58}$$

Near u_∞ take $h_+(u)$ and the root $\sqrt{h(u)/h_\infty}$ equal to one at $u = u_\infty$, and define

$$J_L(u) = \frac{11\sqrt{17}-3}{32}(1+2u)\sqrt{\frac{h(u)}{h_\infty}}\,[1+u-h(u)], \qquad G_L(u) = \frac{\mathcal{B}(u)}{4J_L(u)}, \qquad H_L(u) = \frac{\mathcal{A}(u)^2}{J_L(u)}. \tag{59}$$

Then $\tau = G_L(u)$ and the required function is $H_L(u(\tau))$, with $G_L(u_\infty) = 0$, $H_L(u_\infty) = 1$ and $G_L'(u_\infty) = (187+3\sqrt{17})/128 \neq 0$. The Lagrange–Bürmann formula [44] gives, for $n \geq 1$,

$$b_n = \frac{1}{n}[\xi^{n-1}]\,H_L'(u_\infty+\xi)\left[\frac{\xi}{G_L(u_\infty+\xi)}\right]^n, \tag{60}$$

where $[\xi^m]$ denotes the coefficient of ξ^m. All coefficients lie in the ring

$$b_n \in \mathbb{Z}[1/34, \sqrt{17}]. \tag{61}$$

The reason is arithmetic. The elements inverted in the expansion about the limiting point have norms $N(u_\infty) = -1/4$ and $N(h_\infty) = -1/2$, so only powers of 2 enter there. Formal inversion then determines each new coefficient by division by $G_L'(u_\infty)$, whose norm is $17/8$. Hence 2 and 17 are the only primes in the denominators. The first 13 coefficients obtained by inversion were checked independently by direct substitution into F.

6.7 Two exact radii

The small and the large series are limited by different complex singularities of the same curve (figure 8(a)). Let

$$\chi_\pm = -\frac{787 \pm 99\sqrt{33}}{578}, \qquad \mu_\pm = \frac{85518 \pm 14894\sqrt{33}}{2601}, \qquad P_s = \frac{\chi_- - \sqrt{\chi_-^2 - 4\mu_-}}{2} < 0. \tag{62}$$

Theorem 5 (Radii on the selected sheets)**.** *The small series* (50) *has the exact radius* $|z_s|$*, set by its singularity at* $z_s = P_s/4 < 0$*:*

$$|z_s| = -P_s/4 = 0.104007001009\ldots, \qquad Pe_s = 2\pi\sqrt{-P_s} = 4.052669154822\ldots, \tag{63}$$

and converges absolutely for $|Pe| \le Pe_s$. *The large series* (58), *continuing the positive branch of the threshold, has radius* $|\tau_c| = 1/(2X\mu_+^{1/4}) = 0.138210845046\ldots$, *set by its complex-conjugate singularities* τ_c, *that is*

$$Pe_c = 2\pi\mu_+^{1/4} = 17.893405923407\ldots, \tag{64}$$

and converges absolutely for $|Pe| \ge Pe_c$.

Figure 8(a) shows the regions of convergence. Figure 8(b) compares short truncations with the exact threshold.

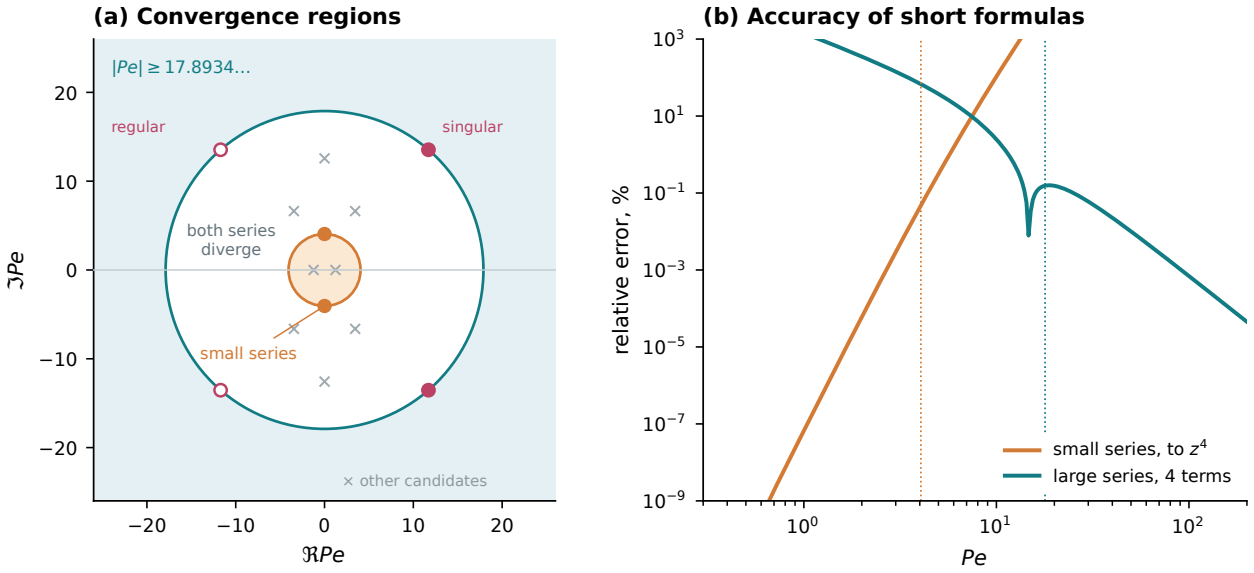


Figure 8: Convergence and accuracy of the series. (a) The small series converges inside the small disk of the complex Pe plane and the large one outside the large disk. Filled points on the outer circle are singular for the selected large sheet, open points are regular, crosses are other candidates from the discriminant. (b) Errors of short truncations relative to the exact threshold; the dip near $Pe \approx 14.8$ is a sign change of the large-series error. Vertical lines mark the radii of convergence; the threshold remains analytic. Between them both series diverge and the threshold is given by $F = 0$, the parametrization (43) or Algorithm 1. The figure was drawn with the AI-assisted Python code described under Computational methods.

The complete proof, with the rational certificates, is given in appendix B; it has two steps. The discriminant lists the possible critical values; one must then establish which of them belong to the selected sheet. This is the third selection step of the paper, after the saddles in section 3 and the frequency in section 4. At the critical value $0 < P_a = 0.038366588824\ldots < |P_s|$ other branches merge, while the selected branch remains regular, so the radius cannot be read off from the zeros of the discriminant alone. For the small series the singularity lies at negative $z_s = P_s/4$, so the coefficients eventually alternate and have order $|z_s|^{-n}n^{-5/2}$. The ratio of moduli of neighboring coefficients tends to $9.614737\ldots$. The large series has two complex-conjugate singularities $\tau_c = 0.090388\ldots \pm 0.104557\ldots\mathrm{i}$, which produce oscillations of the coefficients with the same power correction $n^{-5/2}$. The exponent comes from ordinary cusps of the algebraic projection, whose local expansion has a nonzero term of power 3/2 [45].

At these cusps, $D = D_\kappa = D_{\kappa\kappa} = 0$ and $D_{\kappa\kappa\kappa} \neq 0$: three spatial roots coalesce at an EP3. These are cusps of the projected curve $F = 0$; they should not be confused with the cusp points of the map $\kappa \mapsto \Lambda$ in the frequency plane [31], which are images of simple saddles. Such third-order spatial degeneracies were described as super branch points in rotating-disk flow [46] and discussed by Ó Náraigh and Spelt [34]. In the Prats problem their complex locations limit the selected threshold series; no such coalescence occurs for real $r > 1$, $p > 0$.

On the positive real axis the saddle stays simple and the threshold analytic at Pe_s and Pe_c; both radii are properties of the series alone. These numbers answer a computational question: how far the small series can be used, and from which throughflow the large one converges.

7 What carries over to general rational symbols, and limitations

The argument has three model-dependent steps. (i) Locate all saddles and show that they stay simple on the parameter domain. (ii) Compute the intersection indices at one convenient point (here $p \downarrow 0$, where the physical pair emerges from the real temporal maxima) and prove that they cannot change: no coalescence, and no Stokes phenomenon involving a contributing saddle. (iii) Show that the selected growth is strictly monotone in the forcing parameter, so the threshold is a unique root; elimination and geometry then give the exact boundary. For the symbols of section 5 step (ii) rests on the reflection symmetry $L(-\overline{\kappa}) = \overline{L(\kappa)}$, which turns a possible Stokes phenomenon of the off-axis pair into a perfect square of the spatial quartic, and on the phase structure of the imaginary saddles. For a general rational symbol the first question is therefore the global structure of the physical saddles. Where a symmetry argument is unavailable, rational certificates of the kind used in appendix B can certify the continuation of roots, while the control of Stokes alignments and of relative homology remains separate.

For the power-law fluid, the results apply to transverse rolls. The competition with longitudinal and oblique rolls [16] involves two horizontal wavenumbers and is not covered. In a rectangular anisotropic channel the spanwise modes, $r \neq 0$ in [17], give a two-parameter family of symbols outside the class. Rheologies with a time-dependent momentum response change the structure of the symbol.

A horizontal temperature gradient also changes the symbol. With symmetric wall heat fluxes and an inclined throughflow [20], the dispersion relation comes from a numerical eigenvalue problem. Admissibility has so far been checked there in sample cases. For three-dimensional localized disturbances in a layer with an inclined temperature gradient and vertical throughflow, see Brevdo [47]. A certified global selection for numerically defined dispersion relations would be the natural next step. Finally, the analysis is linear and concerns unbounded layers. Relating the local absolute threshold to global modes or nonlinear fronts in finite domains [4, 5, 48] requires separate treatment, as do porous media beyond the Darcy description [49].

8 Conclusions

For Darcy flow, a horizontal throughflow leaves the onset of growth unchanged and moves the growth away from a fixed observer. The temporal threshold remains $4\pi^2$, whereas the absolute threshold increases with the throughflow. At the absolute threshold the trailing edge of the wavepacket stops, while the crests keep moving.

The same off-axis pair determines the large-time growth of the Green function throughout the domain $r > 1$, $p > 0$. The exact threshold can then be computed in three ways: as the root of a monotone function, as the selected branch of $F = 0$, or along the elliptic arc. The polynomial

gives exact crossings, the arc covers all throughflows, and the two series cover weak and strong throughflow. The certified radii show where each series stops converging, while the threshold itself stays analytic. The examples show three sources of ambiguity: noncontributing saddles, roots added by frequency elimination, and neutral imaginary saddles below the threshold.

The porous convection models share one growth function. For transverse rolls, Forchheimer drag, the power-law index, permeability anisotropy and magnetic resistance enter through the two coefficients of the linearized drag. An open boundary changes the admissible vertical wavenumbers, and interphase heat exchange shifts the level in the metallic foam model. At fixed throughflow the absolute threshold increases with either drag coefficient. This explains why a vertical magnetic field raises the threshold at prescribed Pe, even when curves plotted against the imaginary saddle wavenumber cross.

Table 3 collects the closed-form results of the paper.

Quantity	Closed form
Temporal threshold	$Ra_T = 4\pi^2$ [1]; $\mathcal{R}_T = \pi^2(\sqrt{A}+\sqrt{B})^2$ by scaling, with the anisotropic and magnetic forms in [15, 17]
Neutral saddle locus	Equation and radical parametrization for Prats flow and a vertical magnetic field [15]; here: quadratic form in h for all levels and selection of the physical arc (on 11a3 at $s = 0$)
Weak throughflow	Leading $1 + z$, $z = Pe^2/(16\pi^2)$ [6, 7]; here: $Ra_\mathrm{a}/(4\pi^2) = 1 + z - z^2 + 3z^3 - \cdots \in \mathbb{Z}[[z]]$
Strong throughflow	c_1 known [13–15], c_0 estimated in [18]; exact c_0, c_{-1}, c_{-2} in (55), all b_n by Lagrange–Bürmann, $b_n \in \mathbb{Z}[1/34, \sqrt{17}]$
Limiting saddle	$\kappa_\infty = \frac{1}{4}\sqrt{7+\sqrt{17}} - \frac{\mathrm{i}}{4}\sqrt{5+3\sqrt{17}}$ [13]
General two-term law	Equation (56); the leading Forchheimer and magnetic terms are known from [14, 15], respectively
Crossing with $Ra = Pe^2/4$	numerical value [14, pp. 192–193]; here: $Pe_\times = \frac{\pi}{2}\sqrt{71+17\sqrt{17}} = 18.6583\ldots$, $\kappa_\times = -\mathrm{i}\,\overline{\kappa_\infty}$
Projection node	new: $(Pe, Ra) = (63.78756623,\ 263.08495654)$, crossed smoothly
Radical switch	new: $4u_D^3 + 4u_D^2 - 1 = 0$, $Pe_D = 34.216\ldots$
Radii	new: $Pe_s = 2\pi\sqrt{-P_s} = 4.0527\ldots$, $Pe_c = 2\pi\mu_+^{1/4} = 17.8934\ldots$ (theorem 5, appendix B)
Limits in the class	$r_s(0) = (1+\sqrt{1+s})^2$, the scaled temporal threshold [15, 17]; anisotropy $a \to 0$: $R_\mathrm{a} \to \pi^2$ [17]; open boundary $Ra_\mathrm{a}^\mathrm{BC}(Pe) = \frac{1}{4}Ra_\mathrm{a}(2Pe)$ [13]

Table 3: Closed-form results and their relation to previous work.

Computational methods

ChatGPT (OpenAI, GPT 6.1 Sol) and Claude (Anthropic, Claude Opus 5.5) assisted with algebraic derivations and symbolic checks and with writing and debugging the numerical, verification, and plotting scripts. The author directed this work by specifying the mathematical tasks and the checks to be performed, and reviewed the derivations, code, and numerical results. The verification suite (`prats_check.py`) tests exact algebraic identities, compares series coefficients obtained by independent constructions, checks both convergence certificates using rational arithmetic, and checks saddle selection by contour continuation and by direct quadrature of (4). It also compares the computed thresholds with published benchmarks. The figures were drawn by executing the Python plotting scripts on the specified geometry, computed results, and tabulated benchmarks.

Acknowledgments

This work was supported by the British Academy (Pump Priming Collaboration between UK and EU Partners 2026, award PPHE26\100263). The author acknowledges support of the Institut Henri Poincaré (UAR 839 CNRS-Sorbonne Université), and LabEx CARMIN (ANR-10-LABX-59-01).

The author thanks Michael Berry for suggesting a direct numerical evaluation of the Fourier integral (4).

The AI tools identified under Computational methods also assisted with drafting and editing the text. The author reviewed and edited their output and takes responsibility for the final manuscript.

Declaration of interests

The author reports no conflict of interest.

Data availability statement

The Python scripts, benchmark data, and rational certificate files will be deposited on Zenodo with a persistent identifier (DOI) upon publication.

A Boundary polynomial and frequency recovery

The independent algebraic computation uses $P = p^2/4$ and the polynomial

$$\begin{aligned} F(r,P) = {} & 1024P^5 - 107P^4r^2 - 6464P^4r - 4096P^4 - 8P^3r^4 + 740P^3r^3 \\ & + 14564P^3r^2 - 40832P^3r + 6144P^3 + 48P^2r^5 - 1824P^2r^4 - 7664P^2r^3 \\ & + 63104P^2r^2 - 70976P^2r - 4096P^2 - 96Pr^6 + 2272Pr^5 - 7328Pr^4 \\ & - 12384Pr^3 + 45952Pr^2 - 12800Pr + 1024P + 64r^7 - 1024r^6 \\ & + 5504r^5 - 10496r^4 + 3136r^3 - 256r^2. \end{aligned} \tag{65}$$

With $W = \Omega^2$,

$$\frac{\Delta(\mathrm{i}\Omega)}{16} = \mathcal{U}(W) + \mathrm{i}\Omega\,\mathcal{V}(W), \qquad \mathcal{U}(W) = e_2W^2 + e_1W + e_0, \qquad \mathcal{V}(W) = W^2 + f_1W + f_0,$$

with coefficients

$$\begin{aligned} e_2 &= P - 4r + 1, \\ e_1 &= 8P^2 - 3Pr^2 + 22Pr + 8P + 4r^3 - 22r^2 + 8r, \\ e_0 &= 16P^3 + P^2r^2 - 40P^2r + 16P^2 - 2Pr^3 + 32Pr^2 - 32Pr + r^4 - 8r^3 + 16r^2, \\ f_1 &= 3Pr + 8P - 6r^2 + 12r, \\ f_0 &= -20P^2r + 16P^2 - Pr^3 + 32Pr^2 - 48Pr + r^4 - 12r^3 + 32r^2. \end{aligned} \tag{66}$$

The common root is recovered as

$$W = (r - P)\frac{K_W}{J_W}, \qquad J_W = 3P^2 - 15Pr - 39P + 20r^2 - 32r + 4, \tag{67}$$

$$K_W = -20P^2 - Pr^2 + 91Pr - 92P + 4r^3 - 48r^2 + 132r - 16.$$

When $J_W = 0$ the common roots are found directly from the two quadratics; this covers the node and the crossing with $r = P$, where the fraction may take the form $0/0$. The physical choice always requires $W > 0$.

B Certification of the radii

The discriminant of F with respect to r factorizes as

$$\operatorname{Disc}_r F = 2^{36} P^3 (P+4)^5 Q_2(P) Q_4(P)^3 N_6(P)^2, \tag{68}$$

where

$$Q_2 = 8P^2 + 13P + 16, \qquad Q_4 = 7803P^4 + 21249P^3 + 520020P^2 + 193536P - 8192,$$
$$N_6 = 9P^6 + 435P^5 + 18916P^4 - 16271616P^3 - 15442432P^2 - 22840320P + 100352.$$

The factor N_6^2 corresponds to nodes of the projection, not to branching of the normalization; one of these nodes is discussed in section 4. For the choice of sheet it is convenient to eliminate h from the elliptic model:

$$K_7(u,P) = (4u^2+u-1)^2 P^2 + 4u(2u-1)(2u+1)^2 P + 16u^3(2u+1)^4. \tag{69}$$

The leading coefficient in u is 256, so no root escapes to infinity at finite P, and

$$\operatorname{Disc}_u K_7 = 2^{36} P^9 (P+4)(4P-9)^2 Q_2 Q_4. \tag{70}$$

The four relevant critical values come from the factorization

$$Q_4 = 7803\,(P^2 - \chi_+ P + \mu_+)(P^2 - \chi_- P + \mu_-). \tag{71}$$

The pair with the plus sign is complex conjugate. The factor with the minus sign has two real roots $P_s < 0 < P_a$ with $P_a = 0.038366588824\ldots < |P_s|$; the closer point P_a belongs to another sheet and does not limit the small series. At the critical points of Q_4

$$6u^2 - 3u - 1 = 0. \tag{72}$$

On the smooth elliptic curve the first derivatives of P and r with respect to a local parameter vanish there, while the vectors of second and third derivatives are linearly independent; at such a critical value P_c, after subtracting the analytic part, a nonzero term $(P - P_c)^{3/2}$ remains.

To choose the sheet we use Rouché's theorem [50]. Let $K(w_0 + \xi) = \sum_j \beta_j \xi^j$. If on a disk of radius δ

$$|\beta_\ell| \delta^\ell > \sum_{j \neq \ell} |\beta_j| \delta^j, \tag{73}$$

the disk contains exactly ℓ roots counted with multiplicity. The coefficients are enclosed in rational intervals, and the strict inequality is checked without floating-point rounding; neighboring segments are joined by a smaller disk containing the same single root.

For the small series the substitution $u = Pv$ gives $K_7(Pv, P)/P^2 = 1 - 4v + O(P)$, so the physical germ has $v(0) = 1/4$. A chain of rational segments reaches P_a and keeps the simple positive root u; the roots merging there have $u = (3 - \sqrt{33})/12 < 0$. Loops around $P = 0$ and $P = P_a$ do not change the selected root, and these are all the critical values inside $|P| < |P_s|$; its monodromy is trivial and it is holomorphic in the whole disk. The function r has no poles at finite P, because the leading coefficient of F in r is constant. A further chain reaches the double root at $P = P_s$; the terminal disk contains exactly two roots, and the check (72) establishes the nonzero term of power $3/2$. This proves that the small radius is exact.

For the large series the substitution $P = 1/(4X^2\tau^2)$ turns (69) into a polynomial equation in u, τ. The complex roots of Q_4 have the largest modulus among the finite nonzero critical values

and therefore give the smallest possible nonzero modulus of τ. For $0 < |\tau| < |\tau_c|$ there are no multiple roots and the leading coefficient $256\tau^4$ does not vanish; our germ is analytic at $\tau = 0$, and a loop around the origin does not change it, so inside the disk the selected branch is single-valued and holomorphic. A chain of rational segments brings it to one of the conjugate cusps, and a further chain proves regularity at the point with the opposite sign of τ; the remaining two points follow by conjugation. The two certificates consist of 114 and 403 rational segments, with relative margin in Rouché's inequality above $1/500$. The script `prats_certify.py` verifies the certificates. The exponent $3/2$ gives coefficients of order $n^{-5/2}$, so both series also converge absolutely on the boundaries of their disks.

References

[1] M. Prats, The effect of horizontal fluid flow on thermally induced convection currents in porous mediums, *J. Geophys. Res.* **71**, 4835–4838 (1966). doi:10.1029/JZ071i020p04835

[2] R. J. Briggs, *Electron-Stream Interaction with Plasmas* (MIT Press, Cambridge, MA, 1964). doi:10.7551/mitpress/2675.001.0001

[3] A. Bers, Space-time evolution of plasma instabilities — absolute and convective, in *Basic Plasma Physics I*, ed. A. A. Galeev and R. N. Sudan, Handbook of Plasma Physics, Vol. 1 (North-Holland, Amsterdam, 1983), pp. 451–517.

[4] P. Huerre and P. A. Monkewitz, Local and global instabilities in spatially developing flows, *Annu. Rev. Fluid Mech.* **22**, 473–537 (1990). doi:10.1146/annurev.fl.22.010190.002353

[5] J.-M. Chomaz, Global instabilities in spatially developing flows: non-normality and nonlinearity, *Annu. Rev. Fluid Mech.* **37**, 357–392 (2005). doi:10.1146/annurev.fluid.37.061903.175810

[6] F. Dufour and M.-C. Néel, Numerical study of instability in a horizontal porous channel with bottom heating and forced horizontal flow, *Phys. Fluids* **10**, 2198–2207 (1998). doi:10.1063/1.869741

[7] T. J. Chung, M. C. Kim and C. K. Choi, The spatiotemporal instability on mixed convection in porous media, *Korean J. Chem. Eng.* **26**, 332–338 (2009). doi:10.1007/s11814-009-0056-3

[8] A. Delache, M. N. Ouarzazi and M. Combarnous, Spatio-temporal stability analysis of mixed convection flows in porous media heated from below: comparison with experiments, *Int. J. Heat Mass Transfer* **50**, 1485–1499 (2007). doi:10.1016/j.ijheatmasstransfer.2006.08.040

[9] A. Delache, *Étude analytique et numérique des instabilités spatio-temporelles des écoulements de convection mixte en milieu poreux: comparaison avec l'expérience*, PhD thesis, Université des Sciences et Technologies de Lille (2005). https://pepite-depot.univ-lille.fr/LIBRE/Th_Num/2005/50376-2005-Delache.pdf

[10] E. Diaz and L. Brevdo, Absolute/convective instability dichotomy at the onset of convection in a porous layer with either horizontal or vertical solutal and inclined thermal gradients, and horizontal throughflow, *J. Fluid Mech.* **681**, 567–596 (2011). doi:10.1017/jfm.2011.220

[11] S. C. Hirata and M. N. Ouarzazi, Three-dimensional absolute and convective instabilities in mixed convection of a viscoelastic fluid through a porous medium, *Phys. Lett. A* **374**, 2661–2666 (2010). doi:10.1016/j.physleta.2010.04.039

[12] A. Barletta and L. S. de B. Alves, Absolute instability: a toy model and an application to the Rayleigh–Bénard problem with horizontal flow in porous media, *Int. J. Heat Mass Transfer* **104**, 438–455 (2017). doi:10.1016/j.ijheatmasstransfer.2016.08.052

[13] A. Barletta and M. Celli, Convective to absolute instability transition in a horizontal porous channel with open upper boundary, *Fluids* **2**, 33 (2017). doi:10.3390/fluids2020033

[14] A. Barletta, *Routes to Absolute Instability in Porous Media* (Springer, Cham, 2019). doi:10.1007/978-3-030-06194-4

[15] M. Turkyilmazoglu, Uniform magnetic field impact on absolute versus convective onset of Darcy–Bénard convection with horizontal throughflow, *Int. J. Numer. Methods Heat Fluid Flow* **33**, 3056–3070 (2023). doi:10.1108/HFF-04-2023-0213

[16] L. S. de B. Alves and A. Barletta, Convective to absolute instability transition in the Prats flow of a power-law fluid, *Int. J. Therm. Sci.* **94**, 270–282 (2015). doi:10.1016/j.ijthermalsci.2015.03.009

[17] M. Celli and A. Barletta, Effects of anisotropy on the transition to absolute instability in a porous medium heated from below, *Phys. Fluids* **34**, 024105 (2022). doi:10.1063/5.0085077

[18] A. Barletta, On Prats' problem with anomalous diffusion, *J. Fluid Mech.* **1032**, A18 (2026). doi:10.1017/jfm.2026.11383

[19] A. Barletta, M. Celli, P. V. Brandão and L. S. de B. Alves, Wavepacket instability in a rectangular porous channel uniformly heated from below, *Int. J. Heat Mass Transfer* **147**, 118993 (2020). doi:10.1016/j.ijheatmasstransfer.2019.118993

[20] M. Celli, A. Barletta and P. V. Brandão, Absolute instability in a horizontal porous layer with symmetric wall heat fluxes, *Phys. Fluids* **37**, 094131 (2025). doi:10.1063/5.0290854

[21] R. B. Freitas, P. V. Brandão, L. S. de B. Alves, M. Celli and A. Barletta, The effect of local thermal non-equilibrium on the onset of thermal instability for a metallic foam, *Phys. Fluids* **34**, 034105 (2022). doi:10.1063/5.0083045

[22] S. A. Suslov, Numerical aspects of searching convective/absolute instability transition, *J. Comput. Phys.* **212**, 188–217 (2006). doi:10.1016/j.jcp.2005.06.017

[23] L. S. de B. Alves, S. C. Hirata, M. Schuabb and A. Barletta, Identifying linear absolute instabilities from differential eigenvalue problems using sensitivity analysis, *J. Fluid Mech.* **870**, 941–969 (2019). doi:10.1017/jfm.2019.275

[24] R. J. Deissler, Spatially growing waves, intermittency, and convective chaos in an open-flow system, *Physica D* **25**, 233–260 (1987). doi:10.1016/0167-2789(87)90103-5

[25] F. Pham, *Introduction à l'étude topologique des singularités de Landau*, Mémorial des Sciences Mathématiques **164** (Gauthier-Villars, Paris, 1967).

[26] F. Pham, Vanishing homologies and the n variable saddlepoint method, in *Singularities, Part 2*, Proc. Sympos. Pure Math. **40**, 319–333 (American Mathematical Society, Providence, RI, 1983). doi:10.1090/pspum/040.2/713258

[27] M. V. Berry and C. J. Howls, Hyperasymptotics for integrals with saddles, *Proc. R. Soc. Lond. A* **434**, 657–675 (1991). doi:10.1098/rspa.1991.0119

[28] E. Delabaere and C. J. Howls, Global asymptotics for multiple integrals with boundaries, *Duke Math. J.* **112**, 199–264 (2002). doi:10.1215/S0012-9074-02-11221-6

[29] M. Holzer and A. Scheel, Criteria for pointwise growth and their role in invasion processes, *J. Nonlinear Sci.* **24**, 661–709 (2014). doi:10.1007/s00332-014-9202-0

[30] L. S. Hall and W. Heckrotte, Instabilities: convective versus absolute, *Phys. Rev.* **166**, 120–128 (1968). doi:10.1103/PhysRev.166.120

[31] K. Kupfer, A. Bers and A. K. Ram, The cusp map in the complex-frequency plane for absolute instabilities, *Phys. Fluids* **30**, 3075–3082 (1987). doi:10.1063/1.866483

[32] A. Barletta, Time-evolving to space-evolving Rayleigh–Bénard instability of a horizontal porous medium flow, *Phys. Fluids* **33**, 124106 (2021). doi:10.1063/5.0076368

[33] O. N. Kirillov, *Nonconservative Stability Problems of Modern Physics*, 2nd ed. (De Gruyter, Berlin and Boston, 2021). doi:10.1515/9783110655407

[34] L. Ó Náraigh and P. D. M. Spelt, An analytical connection between temporal and spatio-temporal growth rates in linear stability analysis, *Proc. R. Soc. A* **469**, 20130171 (2013). doi:10.1098/rspa.2013.0171

[35] A. V. Shanin, A. I. Korolkov and K. S. Kniazeva, Saddle point method for transient processes in waveguides, *J. Theor. Comput. Acoust.* **30**, 2150018 (2022). doi:10.1142/S2591728521500183.

[36] R. J. Lingwood, On the application of the Briggs' and steepest-descent methods to a boundary-layer flow, *Stud. Appl. Math.* **98**, 213–254 (1997). doi:10.1111/1467-9590.00048

[37] W. van Saarloos, Front propagation into unstable states, *Phys. Rep.* **386**, 29–222 (2003). doi:10.1016/j.physrep.2003.08.001

[38] R. P. Brent, An algorithm with guaranteed convergence for finding a zero of a function, *Comput. J.* **14**, 422–425 (1971). doi:10.1093/comjnl/14.4.422

[39] F. Capone and S. Rionero, Porous MHD convection: stabilizing effect of magnetic field and bifurcation analysis, *Ric. Mat.* **65**, 163–186 (2016). doi:10.1007/s11587-016-0258-z

[40] The LMFDB Collaboration, The L-functions and modular forms database, elliptic curve 11.a3, https://www.lmfdb.org/EllipticCurve/Q/11/a/3.

[41] R. Hartshorne, *Algebraic Geometry*, Graduate Texts in Mathematics **52** (Springer, New York, 1977), chapter IV, corollary 2.4. doi:10.1007/978-1-4757-3849-0

[42] G. Eisenstein, Über eine allgemeine Eigenschaft der Reihen-Entwicklungen aller algebraischen Functionen, *Bericht Königl. Preuß. Akad. Wiss. Berlin*, 441–443 (1852).

[43] The OEIS Foundation, The On-Line Encyclopedia of Integer Sequences, `https://oeis.org`; search for the coefficients of (50) and their moduli, 31 October 2026.

[44] P. Flajolet and R. Sedgewick, *Analytic Combinatorics* (Cambridge University Press, 2009). `doi:10.1017/CBO9780511801655`

[45] P. Flajolet and A. Odlyzko, Singularity analysis of generating functions, *SIAM J. Discrete Math.* **3**, 216–240 (1990). `doi:10.1137/0403019`

[46] J. J. Healey, On the relation between the viscous and inviscid absolute instabilities of the rotating-disk boundary layer, *J. Fluid Mech.* **511**, 179–199 (2004). `doi:10.1017/S0022112004009565`

[47] L. Brevdo, Three-dimensional absolute and convective instabilities at the onset of convection in a porous medium with inclined temperature gradient and vertical throughflow, *J. Fluid Mech.* **641**, 475–487 (2009). `doi:10.1017/S0022112009992163`

[48] B. Sandstede and A. Scheel, Absolute and convective instabilities of waves on unbounded and large bounded domains, *Physica D* **145**, 233–277 (2000). `doi:10.1016/S0167-2789(00)00114-7`

[49] D. A. Nield and A. Bejan, *Convection in Porous Media*, 5th edn (Springer, Cham, 2017). `doi:10.1007/978-3-319-49562-0`

[50] NIST Digital Library of Mathematical Functions, §1.10(iv), Rouché's theorem, `https://dlmf.nist.gov/1.10`.